Supporting Information for

POMs@ZIF-8 derived transition metal carbides for urea electrolysis-assisted hydrogen generation

Jianping Zhu, Haibo Wu, Kaige Gui, Zhirong Li, Chao Zhang,* Jingping Wang, and Jingyang Niu*

Henan Key Laboratory of Polyoxometalate Chemistry, Institute of Molecular and Crystal Engineering, College of Chemistry and Chemical Engineering, Henan University, Kaifeng, Henan 475004, P. R. China

Fax: (+ 86)371-23886876
E-mail: zhangchao@henu.edu.cn; jyniu@henu.edu.cn

Results and Discussion

1. Characterization data (**Fig. S1 – S41**)

2. Table results (**Table S1-S6**)

Experimental Section

Chemicals and Reagents

All chemicals were obtained from commercial suppliers and used without further purification unless specified otherwise: zinc nitrate hexahydrate (99%, AR), 2-methylimidazole (2-HmIm, 98%, AR), Triethylamine (TEA, 99%, AR), Methanol (99.5%, AR), N, N-Dimethylformamide (DMF, 99.5%, AR), Nickel nitrate hexahydrate (98%, AR), Cyanoguanidine (DCA, 99%, AR), potassium hydroxide (85%, AR), Urea (99.0%, AR), carbon black (EC600JD), 5 wt% Nafion solution. Commercial Pt/C (20 wt%), Ru/C (5 wt%), and IrO_2 (99.9%) were purchased from Titan Scientific Co, Ltd. (Shanghai, China).

Characterization

FT-IR spectra were obtained on a PerkinElmer infrared spectrometer with the potassium bromide tablet method, and the range was 400 - 4500 cm^{-1}. Liquid ultraviolet-visible (UV-vis) spectra were operated on a Hitachi UV-4100 spectrometer. X-ray powder diffraction (XRD) data were performed on a Bruker D8 Advance X-ray diffractometer equipped with graphite-monochromatized Cu Kα radiation (λ = 1.54 Å). The transmission electron microscope JEM-2100 was used to acquire the electron transmission microscopy (TEM) and high-resolution TEM (HRTEM) images. Scanning electron microscope (SEM) images were carried out on JSM-7610F. The contents of Zn, P, Mo, Si, W and Ni were quantified on Perkin-Elmer Optima 2100 DV inductively coupled plasma atomic emission spectroscopy (ICP-AES). N_2 sorption isotherms were operated on a Quadrasorb SI-4; the Brunauer-Emmett-Teller (BET) surface area and pore sizes were analyzed using ASiQwin software. X-ray photoelectron spectra (XPS) were carried out using a Thermo ESCALAB 250 XI spectrometer and the X-ray source was achromatic Al Kα. The gas product was detected using a PANNA A91Plus gas chromatography equipped with a thermal conductivity detector. Ar was used as a carrier gas, and the flow rate is 20 mL min^{-1}.

Electrochemical measurements

Electrochemical experiments were performed using a standard three-electrode configuration at room temperature. A modified glassy carbon electrode (GC, d = 5 mm), an Ag/AgCl (filled with 3.5 M KCl solution) electrode and a graphite rod electrode served as working electrode, reference electrode, and counter electrode, respectively. The reliability of Ag/AgCl electrode in alkaline solutions was verified (**Fig. S15 – S20**) and employed a salt bridge to protect the Ag/AgCl electrode.

5 mg of the catalysts were dispersed in a mixture of ethanol (0.47 mL) and 5 wt% Nafion (0.03 mL) by sonication to form a homogeneous ink. Typically, 10 μL well-dispersed catalysts (corresponding to a catalyst loading of 0.51 mg cm^{-2}) were covered on the GC electrode and then dried in an ambient environment for measurements. Linear Sweep Voltammetry, Cyclic voltammetry and Chronoamperometry measurements were carried out by using a CHI 660e or CHI 760e electrochemical workstation. Hydrogen evolution reaction (HER) curves data were collected at a scan rate of 5 mV s^{-1} in 1M KOH electrolyte, and urea oxidation reaction (UOR) curves data were collected at a scan rate of 50 mV s^{-1} in 1.0 M KOH with or without 0.33 M urea electrolytes. All the potentials, measured against Ag/AgCl electrode, were converted into the potential versus the RHE according to the Nernst equation: $E_{RHE} = E_{Ag/AgCl} + 0.059\ pH + E^{\theta}_{Ag/AgCl}$.

To estimate the electrochemically active surface areas of the catalysts, CV measurements were carried out in 1.0 M KOH aqueous solution from -0.10 V to 0 V (*vs.* Ag/AgCl, 3.5 M KCl filling solution, Ni/WC@C) and from 0 V to 0.1 V (*vs.* RHE, MoC@C) with scan rates of 5, 10, 25, 50, 100, 200 and 400 mV s^{-1}, respectively. Tafel slopes were determined by fitting the linear regions of the Tafel plots to the Tafel equation ($\eta = b \log (j) + a$) by replotting the polarization curves. Electrochemical impedance spectroscopy (EIS) for Ni/WC@C was performed at 0.35 V (*vs.* Ag/AgCl/3.5 M KCl filling solution) with a frequency range from 100 K Hz to 1 Hz. The EIS spectra were fitted using the ZView2 software.

For the urea electrolysis and water splitting, the MoC@C and Ni/WC@C were used as cathode and anode catalysts, respectively. The scan rate was at 5 mV s^{-1} and the electrolyte was 1.0 M KOH + 0.33 M urea and 1.0 M KOH solution.

Calibration of Reference Electrode

we evaluated the stability of the Ag/AgCl electrode by comparing the open circuit potential (OCP) between it and a saturated calomel electrode (SCE) in a 1 M KOH solution. As shown in **Fig. S15**, the OCP value between the Ag/AgCl electrode and the SCE is stable and the 0.038 V difference between the two electrodes is acceptable (0.244 V for SCE *vs* 0.205 V for Ag/AgCl electrode).

Preparation of the Agar Salt Bridge

The preparation of the salt bridge was based on the previous report with some modifications[1]: KCl (4.47

g, 0.06 mol) was dissolved in 60 mL of deionized water; then agar (0.06 g) was added into the above solution with vigorous stirring. The mixture was heated to a boil to melt agar and prevent it from clotting. Subsequently, the mixed solution containing agar was filled into U-tubes (6 mL), and then agar-filled U-tubes should be immediately placed in fresh 3.5 M KCl to prevent shrinkage of the agar during cooling. When cool, remove any excess agar from the outside of the bridges and examine for bubbles.

The salt bridge installed electrolysis cell was shown in **Fig. S16**. We separated the Ag/AgCl electrode with a salt bridge and verified the reliability of the setup by comparing the CV curves of 5 mM $K_3Fe(CN)_6$ with and without the salt bridge (**Fig. S17**). The results indicate the salt bridge does not affect the electrochemical experiments. We further compared the CV curves of Ni/WC@C in 1 M KOH + 0.33 M urea solution (**Fig. S18**) and LSV curves of MoC@C in 1 M KOH solution with and without the salt bridge (**Fig. S19**). No obvious difference can be observed from these experiments. Then, we re-measured the stability of Ni/WC@C with the salt bridge by chronoamperometry. As demonstrated in **Fig. S20**, the current density loss of UOR for Ni/WC@C after 10 hours of electrolysis is 17.7%, which agrees well with our original result. After the long-term electrolysis, we verified the Ag/AgCl electrode by $K_3Fe(CN)_6$ CV tests again (**Fig. S17**). It can be observed that whether being protected by a salt bridge or not, the Ag/AgCl electrode demonstrates highly stable properties after 10 hours of electrolysis in alkaline solutions.

Determination of Faradaic efficiency

Faradaic efficiency (FE) of MoC@C or Ni/WC@C catalysts is defined as the ratio of the amount of experimentally determined H_2 or N_2 to that of the theoretically expected H_2 or N_2 from the HER or UOR. The gas product was analyzed by gas chromatography. The standard curve for quantitative detection of H_2 or N_2 was determined by an external standard method, and the conditions for the calibration are the same as the conditions for the catalytic reaction.

Typically, the solution of 1 M KOH was continuously electrolyzed at a fixed potential of - 0.15 V (*vs.* RHE) for 12 h by using MoC@C catalyst. The amount of H_2 was determined by gas chromatography at stipulated times (60, 120, 180, 240, 300, 360, 420, 480, 540, 600, 660 and 720 min).

Typically, the solution of 1.0 M KOH + 0.33 M urea was continuously electrolyzed at a fixed potential of 1.45 V (*vs.* RHE) for 10 h by using Ni/WC@C catalyst. The amount of N_2 was determined by gas

chromatography at stipulated times (60, 120, 180, 240, 300, 360, 420, 480, 540 and 600 min).

Determination of the MoC's and Ni/WC's particle distribution from the XRD particles size analysis

We use the Sherrer equation to estimate the MoC and Ni/WC's size on jade software.

$$D=k\lambda/\beta\cos\theta$$

D: grain size (nm); **k**: index, when **β** is the full width at half maxima, **k** is 0.89; **λ**: X-ray wavelength, 0.154 nm; **β**: full width at half maxima, FWHM; **θ**: angle of deviation.[2]

As shown in Table S1 and Table S2, we used the reflections of 34.75 (101), 36.54 (006), 39.37 (103), 42.63 (104), 46.76 (105), 56.38 (107), 61.61 (110), 67.90 (109) and 72.96 (201) to calculate particle diameters of MoC sample with Sherrer equation, and the reflections of 31.37 (001), 35.56 (100), 44.05 (111), 48.38 (101), 64.05 (110), 73.18 (111), 75.47 (200), 77.20 (102) and 84.13 (201) were used to calculate particle diameters of Ni/WC sample.

Calculation results display that the average particle diameters of the MoC and the Ni/WC are 2 – 3 nm which agrees well with the TEM analysis.

Synthesis of samples

α-[(*n*-C_4H_9)$_4$N]$_3$-[$PMo_{12}O_{40}$]·17H_2O (PMo_{12}) was synthesized according to the literature.[3] α-$K_4[SiW_{12}O_{40}]\cdot 17H_2O$ (SiW_{12}) and α-$Na_{10}[SiW_9O_{34}]\cdot 18H_2O$ (SiW_9) were synthesized according to the literature.[4]

Synthesis of α-$K_{10}[SiW_9O_{37}Ni_3(H_2O)_3]$ (SiW_9Ni_3): SiW_9Ni_3 was synthesized based on the literature with some modifications.[5] To a solution of $NiSO_4\cdot 7H_2O$ (3.4 g, 12 mmol) in 0.5 mol L^{-1} sodium acetate (150 mL), SiW_9 (11.2 g, 4 mmol) was slowly added at 70°C. The mixed solution was heated at 90°C for 1 h under stirring. Subsequently, the solution was cooled to room temperature and filtered. An aqueous solution (12 mL) of KCl (4 g) was added slowly to the above filtrate, and then the resulting green precipitate was filtered off and recrystallized in hot water (60°C).

Synthesis of O-ZIF (including ZIF-8, carbon, and DCA): Since PMo_{12} is insoluble in water, to prepare PMo_{12}@ZIF, we prepared ZIF-8 in organic solvent according to literature reports,[6] and named the synthesized ZIF-8 in an organic solvent as O-ZIF for differentiation. The 2-HmIm (3.7 g, 45.10 mmol) and carbon black (0.1 g) were dissolved or dispersed in MeOH (56 mL) and DMF (24 mL) with vigorous stirring. Then, a solution (24 mL DMF + 56 mL CH_3OH) of $Zn(NO_3)_2\cdot 6H_2O$ (1.68 g, 5.60 mmol), DCA (3.6g, 42.80 mmol) simultaneously and slowly added to the above mixture solution with vigorous stirring for 24 hours. Gray precipitates were collected by centrifugation and washed with DMF and CH_3OH.

Synthesis of PMo_{12}@ZIF: The 2-HmIm (3.7 g, 45.10 mmol) and carbon black (0.1 g) were dissolved or dispersed in MeOH (56 mL) and DMF (24 mL) with vigorous stirring. Then, a solution (24 mL DMF + 56 mL CH_3OH) of $Zn(NO_3)_2\cdot 6H_2O$ (1.68 g, 5.60 mmol), DCA (3.6 g 42.80 mmol) and PMo_{12} (0.72 g, 0.26 mmol) were simultaneously and slowly added to the above mixture solution with vigorous stirring for 24 hours. Gray precipitates were collected by centrifugation and washed with DMF and CH_3OH.

Synthesis of W-ZIF (ZIF-8 and carbon): Due to all POMs except PMo_{12} in this paper being soluble in water, the yield of ZIF-8 synthesized in an organic solvent is lower, We synthesized ZIF-8 in an aqueous solution according to the previous report.[7] To distinguish, ZIF-8 synthesized in an aqueous solution was denoted as W-ZIF. The 2-HmIm (4.42 g, 53.90 mmol), TEA (2.95 mL) and carbon black (0.1 g) were dissolved or dispersed in deionized water (25 mL) with vigorous stirring. Then, an aqueous solution (20

mL) of $Zn(NO_3)_2 \cdot 6H_2O$ (2 g, 6.70 mmol) was slowly added to the above mixture solution with vigorous stirring for 1 hour. Gray precipitates were collected by centrifugation and washed with deionized water. The product was dried in a vacuum at 60℃ overnight.

Synthesis of SiW_9Ni_3@ZIF: The 2-HmIm (4.42 g, 53.90 mmol), TEA (2.95 mL) and carbon black (0.1 g) were dissolved or dispersed in deionized water (25 mL) with vigorous stirring. Then, an aqueous solution (20 mL) of $Zn(NO_3)_2 \cdot 6H_2O$ (2 g, 6.70 mmol) and an aqueous solution (20 mL) of SiW_9Ni_3 (0.76 g, 0.26 mmol) were simultaneously and slowly added to the above mixture solution with vigorous stirring for 1 hour. Gray precipitates were collected by centrifugation and washed with deionized water. The product was dried in a vacuum at 60℃ overnight.

Synthesis of SiW_{12}@ZIF: SiW_9Ni_3 was replaced by SiW_{12} (0.75 g, 0.26 mmol) could prepare SiW_{12}@ZIF.

Synthesis of SiW_9@ZIF: SiW_9Ni_3 was replaced by SiW_9 (0.75 g, 0.26 mmol) could prepare SiW_9@ZIF.

Synthesis of PMo_{12}/ZIF: The PMo_{12} (0.5 g) and O-ZIF (0.7 g) were mixed and ground uniformly.

Synthesis of Ni-ZIF: The synthesis of Ni-ZIF was similar to ZIF-8, except that $Zn(NO_3)_2 \cdot 6H_2O$ solution was replaced by $Zn(NO_3)_2 \cdot 6H_2O$ (1.71 g, 5.75 mmol)/$Ni(NO_3)_2 \cdot 6H_2O$ (0.24 g, 0.81 mmol) mixture solution.

Synthesis of SiW_{12}@ZIF+Ni-ZIF: The SiW_{12}@ZIF (1.0 g) and Ni-ZIF (0.5 g) were mixed and ground uniformly.

Synthesis of P-ZIF: The synthesis of P-ZIF was similar to SiW_9Ni_3@ZIF, except that SiW_9Ni_3 solution was replaced by Na_2HPO_4 (0.047 g, 0.34 mmol) solution.

Synthesis of Si-ZIF: The synthesis of Si-ZIF was similar to SiW_9Ni_3@ZIF, except that SiW_9Ni_3 solution was replaced by $Na_2SiO_3 \cdot 5H_2O$ (0.127 g, 0.6 mmol) solution.

Synthesis of ZIF-p. The 0.4 g O-ZIF composite was transferred into a temperature-programmed furnace under N_2 flow (40 - 60 mL min^{-1}), heat-treated at 600°C for 3 h, and then at 900 °C for 6 h at a heating rate of 5 °C min^{-1}. The sample was cooled to room temperature naturally under N_2 flow to obtain ZIF-p.

Synthesis of MoC@C: The 0.2 g PMo_{12}@ZIF composite was transferred into a temperature-programmed furnace under a nitrogen flow (50 mL min^{-1}), heat-treated at 900℃ for 6 hours with a heating rate of 5 ℃ min^{-1}. The sample was cooled to room temperature naturally under nitrogen flow to obtain MoC@C.

Synthesis of MoC/C: The synthesis of MoC/C was similar to the synthesis procedure of MoC@C, except the PMo_{12}@ZIF sample was replaced by PMo_{12}/ZIF.

Synthesis of Ni/WC@C: The 0.5 g SiW_9Ni_3@ZIF composite was transferred into a temperature-programmed furnace under a nitrogen flow (40 mL min^{-1}), heat-treated at 900°C for 4 h with a heating rate of 5 °C min^{-1}. The sample was cooled to room temperature naturally under nitrogen flow to obtain Ni/WC@C.

Synthesis of P-ZIF-p, Si-ZIF-p, Ni+WC@C, WC@C, WC/W@C and Ni@C: The synthesis of P-ZIF-p, Si-ZIF-p, Ni+WC@C, WC@C, WC/W@C and Ni@C was similar to the synthesis procedure of Ni/WC@C, except SiW_9Ni_3@ZIF sample was replaced by P-ZIF, Si-ZIF, SiW_{12}@ZIF+Ni-ZIF, SiW_{12}@ZIF, SiW_9@ZIF and Ni-ZIF.

Synthesis of MoO_3@C, WO_3@C and Ni/WO_3@C: MoC@C (0.1 g), WC@C (0.1 g) or Ni/WC@C (0.1 g) was transferred in a temperature-programmed tube furnace under air atmosphere, heat-treated at 500°C for 3 h at a heating rate of 2 °C min^{-1}. The sample was then cooled to room temperature naturally under airflow to obtain MoO_3@C, WO_3@C and Ni/WO_3@C.

Detailed discussions of catalyst synthesis

A series of transition metal carbide NPs were synthesized by a two-step process: In the case of MoC@C. First, PMo_{12} was *in-situ* encapsulated[8] into the cavities of ZIF-8 to obtain PMo_{12}@ZIF precursors. ZIF-8 was chosen as the trapping reagent and the carbon sources of the carbides because its cavities (diameter: 1.1 nm) can perfectly encapsulate Keggin-type POM molecules (diameter: 0.9 nm), and the adjacent cavities can accommodate cations to balance the charge and further separate the POM molecules. In addition, ZIF-8 could protect Mo/W sources from aggregation during the pyrolysis process. The Zn species of the ZIF-8 will evaporate over 900°C, leaving a porous and conductive carbon matrix.[9]

In the synthesis process, the addition of carbon black and DCA aim to increase the carbon and nitrogen content of the PMo_{12}@ZIF. This is to ensure that the TMCs are evenly distributed when applied to the electrode and to increase the electrical conductivity of the product.

The preparation POMs@ZIF precursors were washed several times to remove adsorbed POMs on ZIF-8 nanoparticles (NPs) surfaces. No characteristic O→W UV-vis spectroscopy absorption peak was observed in the supernatant solution of the as-synthesized samples (**Fig. S1)**, indicating the complete removal of adsorbed POMs from the ZIF-8 surfaces. The IR spectrum of the prepared sample show characteristic peaks of PMo_{12} (**Fig. S2a**), confirming the presence of PMo_{12} in the as-synthesized samples. Moreover, The XRD pattern of the prepared sample was in agreement with the simulation results of ZIF-8 (**Fig. S2b**), indicating the integrity of the ZIF-8 framework and confirming the absence of crystalline aggregation of PMo_{12}. Based on these characterizations, we confirm that PMo_{12} clusters have been successfully encapsulated into the cavities of ZIF-8. The as-synthesized sample was denoted as PMo_{12}@ZIF. SEM images showed that the PMo_{12}@ZIF share the same morphology with bare ZIF-8 thus confirming the encapsulation condition which is moderate and does not destroy the nanocrystalline morphology of ZIF-8 during the entire process. (**Fig. S3**). ICP-AES result showed that the Mo contents of PMo_{12}@ZIF are 18.62% (**Table S3).** SiW_{12}@ZIF, SiW_9Ni_3@ZIF, and other samples have also been characterized as PMo_{12}@ZIF (**Fig. S4** – **S5, S27** and **S28**).

Then, the other POMs@ZIF (PMo_{12}@ZIF, SiW_{12}@ZIF, SiW_9Ni_3@ZIF, PMo_{12}/ZIF, SiW_{12}@ZIF+Ni-ZIF, and Ni-ZIF) precursors were pyrolyzed at 900°C under N_2 flow to produce carbide NPs. It should be noted that we did not take 3d metal-modified Mo POMs here because it has been rarely reported.[10] According to XRD results, molybdenum carbide, metallic Ni and tungsten carbide hybrid NPs, tungsten carbide, metallic Ni, molybdenum carbide mixed with carbon, and tungsten carbide mixed with metallic Ni sample were obtained from pyrolyzed PMo_{12}@ZIF, SiW_9Ni_3@ZIF, SiW_{12}@ZIF, Ni-ZIF, PMo_{12}/ZIF, and SiW_{12}@ZIF+Ni-ZIF (**Fig. 2a**, **2c, S22**, and **S29**). They are denoted as MoC@C, WC@C, Ni/WC@C, Ni@C, MoC/C, and Ni+WC@C. It should be noted that there is also a weak diffraction peak at the 2-theta value of 39º in the XRD pattern of Ni/WC@C. To attribute this diffraction peak, we have carefully compared the XRD pattern of the Ni/WC@C with all the standard PDF cards of possible species in our system. As a result, there are only three standard PDF cards that contain diffraction peaks at a 2-theta value of 39° (**Fig. S6a**). They are metallic tungsten (PDF#04-0806), Ni_3C (PDF#06-0697) and NiC_x

(PDF#45-0979). So, the weak diffraction peak at a 2-theta value of 39° in the XRD pattern of the Ni/WC@C can be attributed to either metallic W or Ni carbides. Since we can synthesize single-component (solo Ni or solo WC embedded in the carbon matrixes, i.e. Ni@C and WC@C) under identical synthesis conditions, we then compared the XRD patterns of Ni/WC@C, WC@C, and Ni@C (**Fig. S6b**). As a result, both the XRD patterns of Ni/WC@C and WC@C demonstrated a weak but observable peak at 39°, whereas no peak can be found from the XRD pattern of Ni@C at the same 2-theta value. The Ni-C bonds in nickel carbides are very weak, the Ni_3C begins to decompose at 465°C.[11,12] Considering the pyrolysis temperatures in our synthesis method are 900°C, even if Ni carbides formed during the pyrolysis process, they would decompose at last. So, we attribute the weak 39° XRD peak of the Ni/WC@C to over-reduced the trace amount of W species rather than Ni carbides. In addition, the pyrolyzed samples of ZIF, P-ZIF, and Si-ZIF precursors are denoted as the name of precursors + "-p".

We also synthesized an ex situ sample (MoC/C) by mechanically mixing and grinding PMo_{12} and ZIF precursors, and then pyrolyzing the mixture in the same way as MoC@C (see the synthesize section for more details). The TEM image of MoC/C NPs (**Fig. S22**) revealed the average diameter of MoC in MoC/C to be 7.5 nm, which is 3~4 times larger than that of MoC@C. Notwithstanding the chemical compositions and the contents of the active species of MoC@C and MoC/C being similar (**Fig. S23** and **Table S3**), the HER activity of MoC/C is much poorer than that of MoC@C (**Fig. 3a** and **b** red curves vs. green curves). This result suggests that the carbides suffer from aggregation during the carbonization without the space confinement effect of the cavities of ZIFs, resulting in the low catalytic activity of MoC.

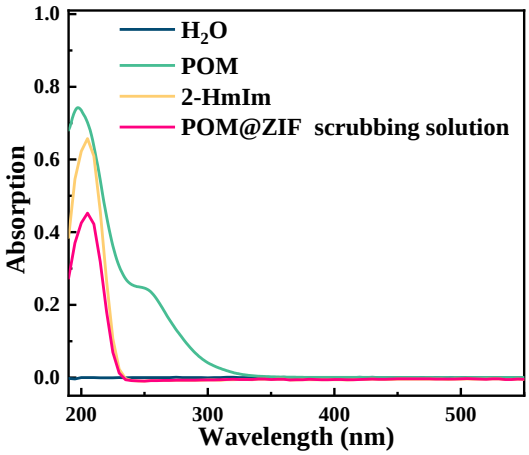

Fig. S1 UV-vis spectra of H_2O, POM, 2-HmIm and POM@ZIF scrubbing solution.

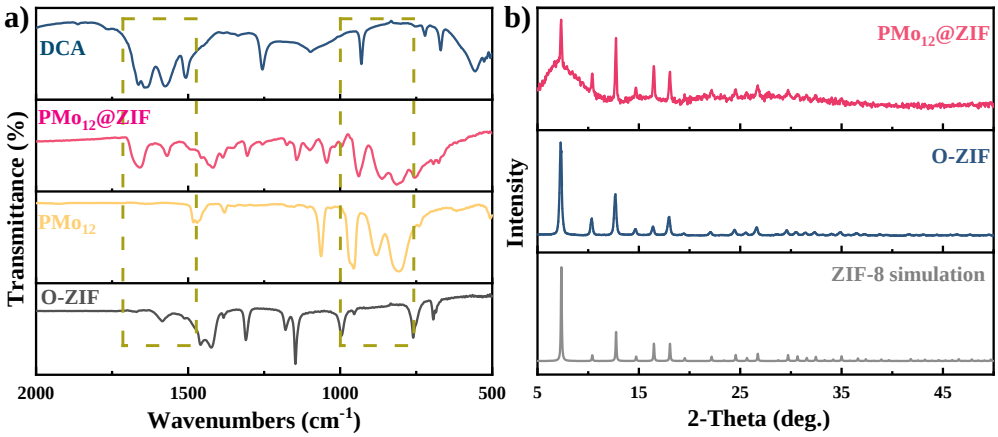

Fig. S2 (a) IR spectrum of O-ZIF, PMo_{12}, PMo_{12}@ZIF and DCA, (b) XRD patterns of ZIF-8 simulation, O-ZIF and PMo_{12}@ZIF.

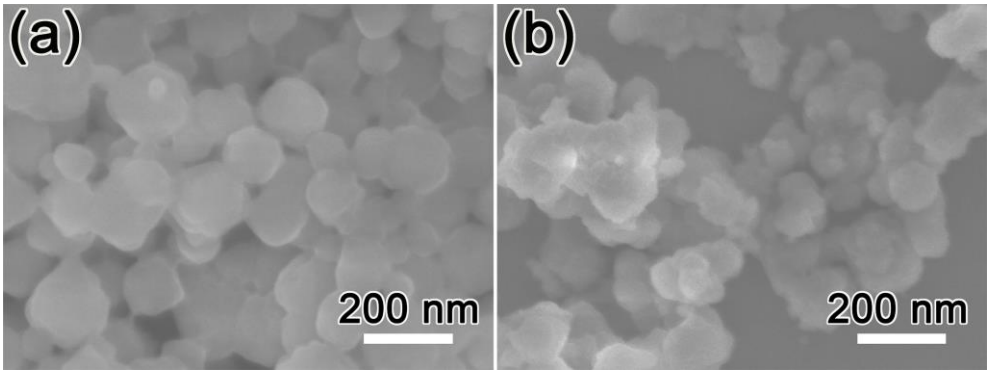

Fig. S3 SEM images of (a) ZIF-8, and (b) PMo_{12}@ZIF samples.

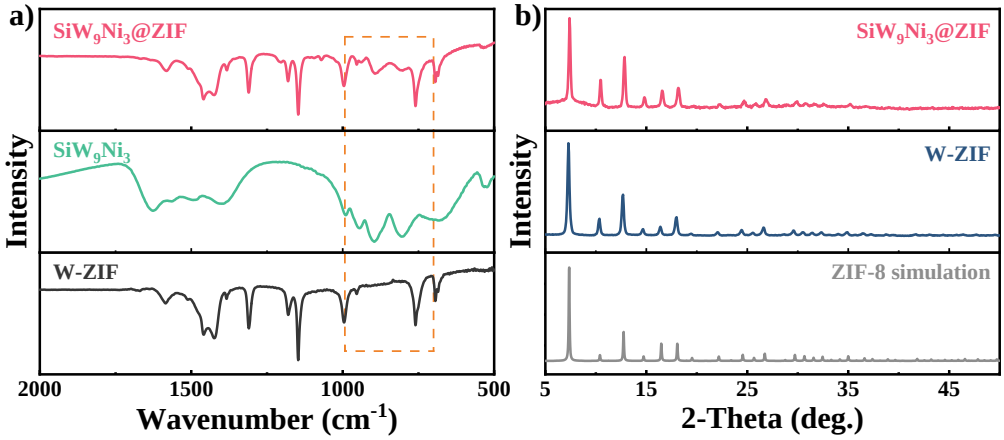

Fig. S4 (a) IR spectrums of W-ZIF, SiW_9Ni_3, and SiW_9Ni_3@ZIF, (b) XRD patterns of ZIF-8 simulation, W-ZIF and SiW_9Ni_3@ZIF.

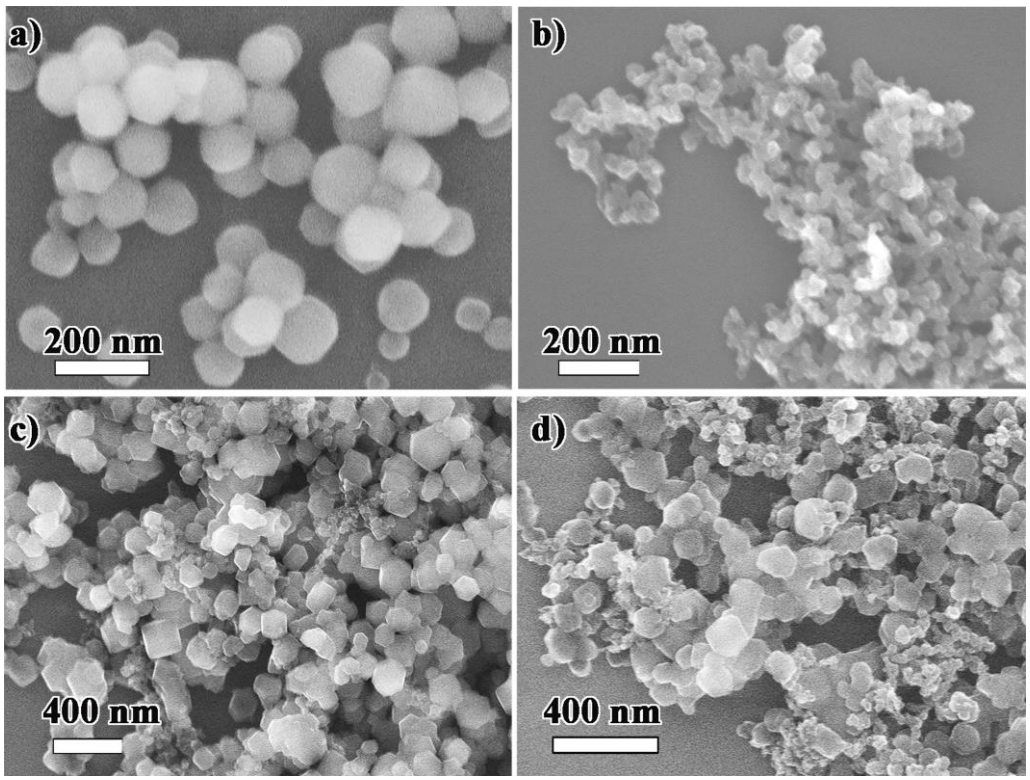

Fig. S5 SEM images of (a) ZIF-8, (b) carbon black, (c) bare ZIF, and (d) SiW_9Ni_3@ZIF samples.

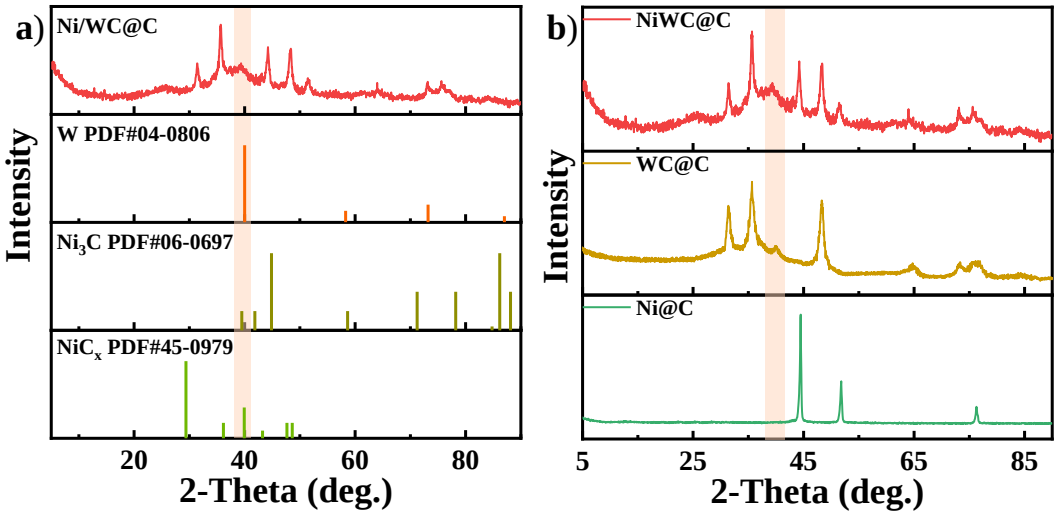

Fig. S6 (a) XRD pattern of Ni/WC@C, (b) XRD patterns of Ni/WC@C, WC@C and Ni@C.

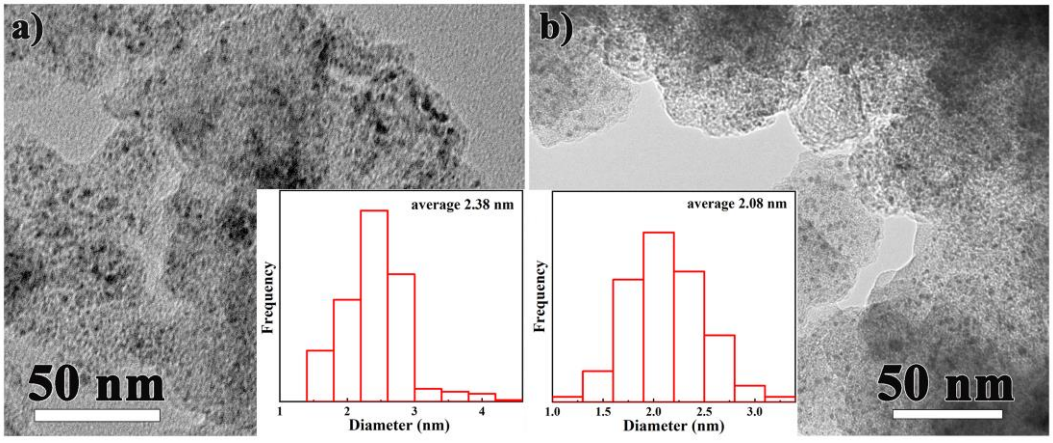

Fig. S7 TEM images of (a) MoC@C, and (b) Ni/WC@C (inset: particle size distribution).

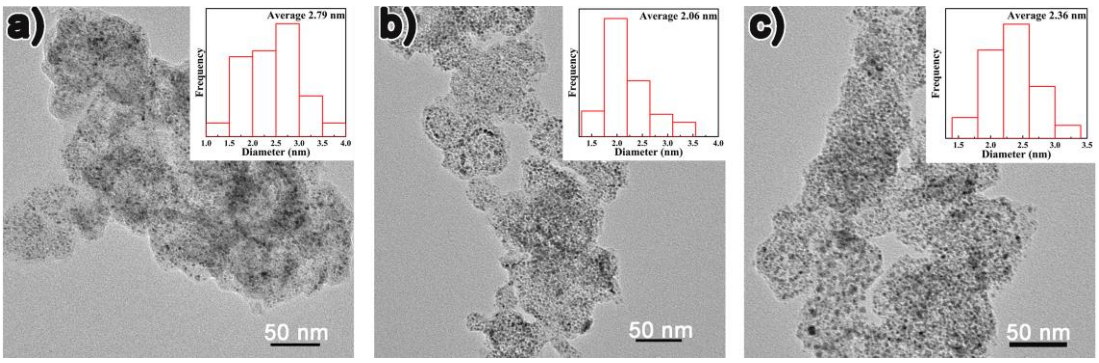

Fig. S8 TEM images of MoC@C (insert: particle size distribution).

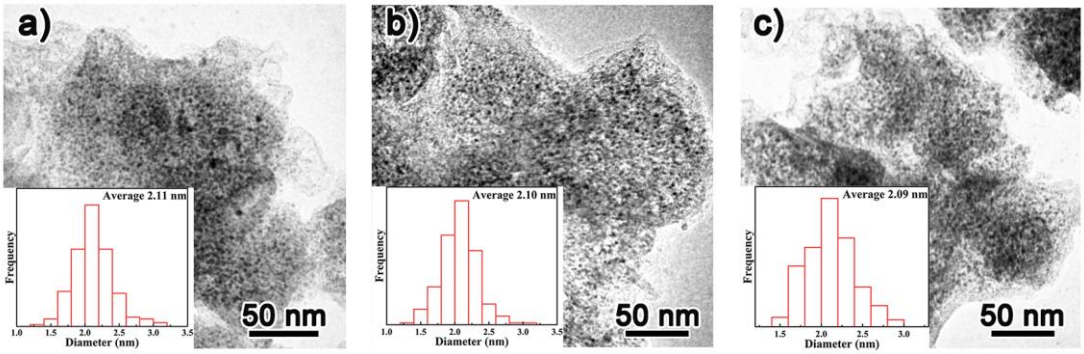

Fig. S9 TEM images of Ni/WC@C (insert: particle size distribution).

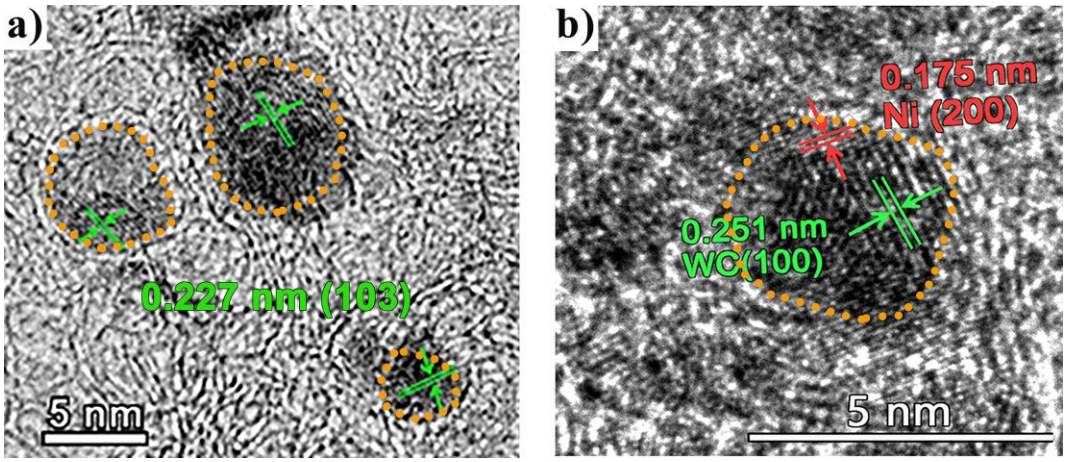

Fig. S10 HRTEM images of (a) MoC@C, (b) Ni/WC@C.

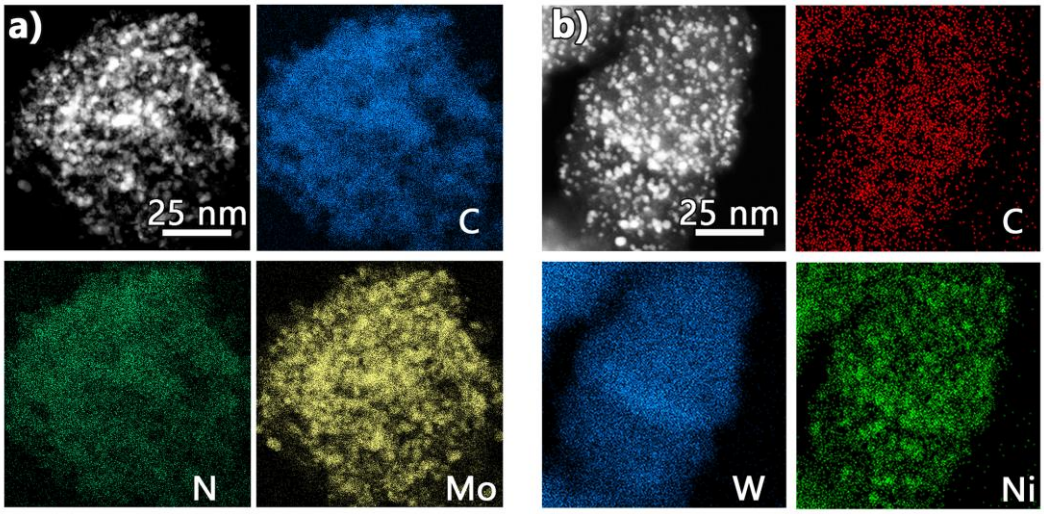

Fig. S11 EDX mapping of (a) MoC@C, (b) Ni/WC@C.

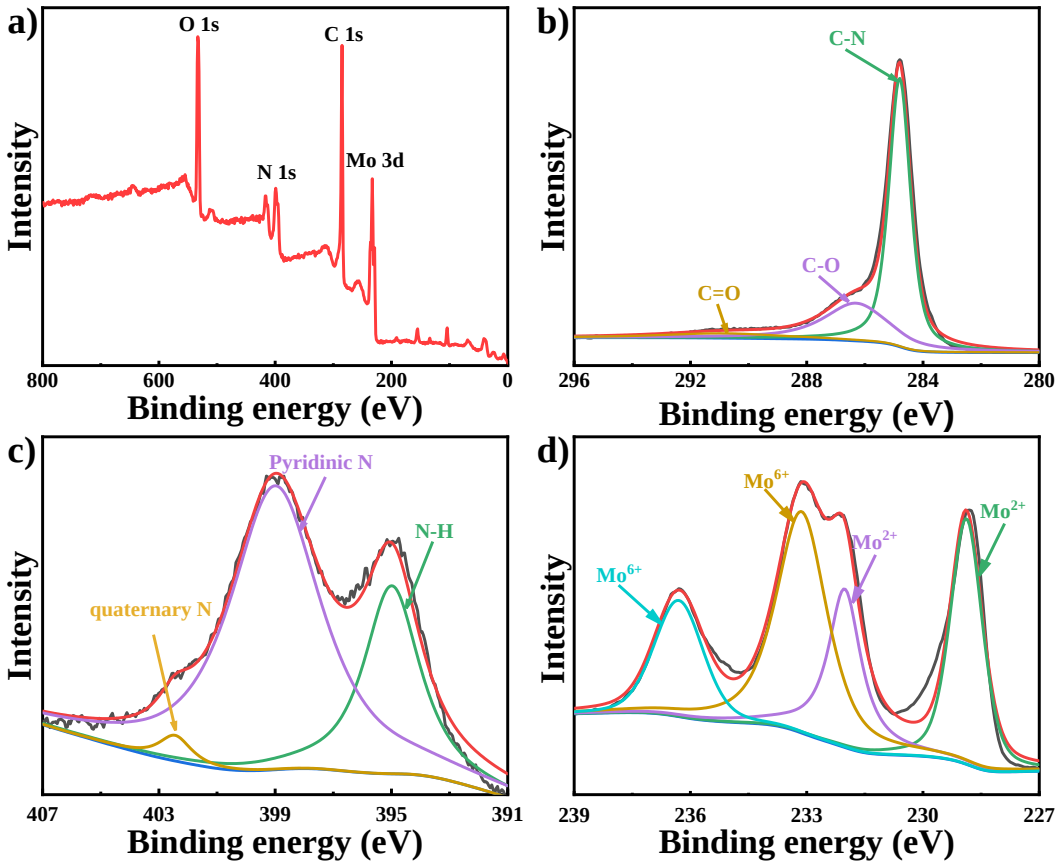

Fig. S12 (a) The survey XPS spectrum of MoC@C; the high-resolution (b) C 1s, (c) N 1s, and (d) Mo 3d XPS spectra of MoC@C.

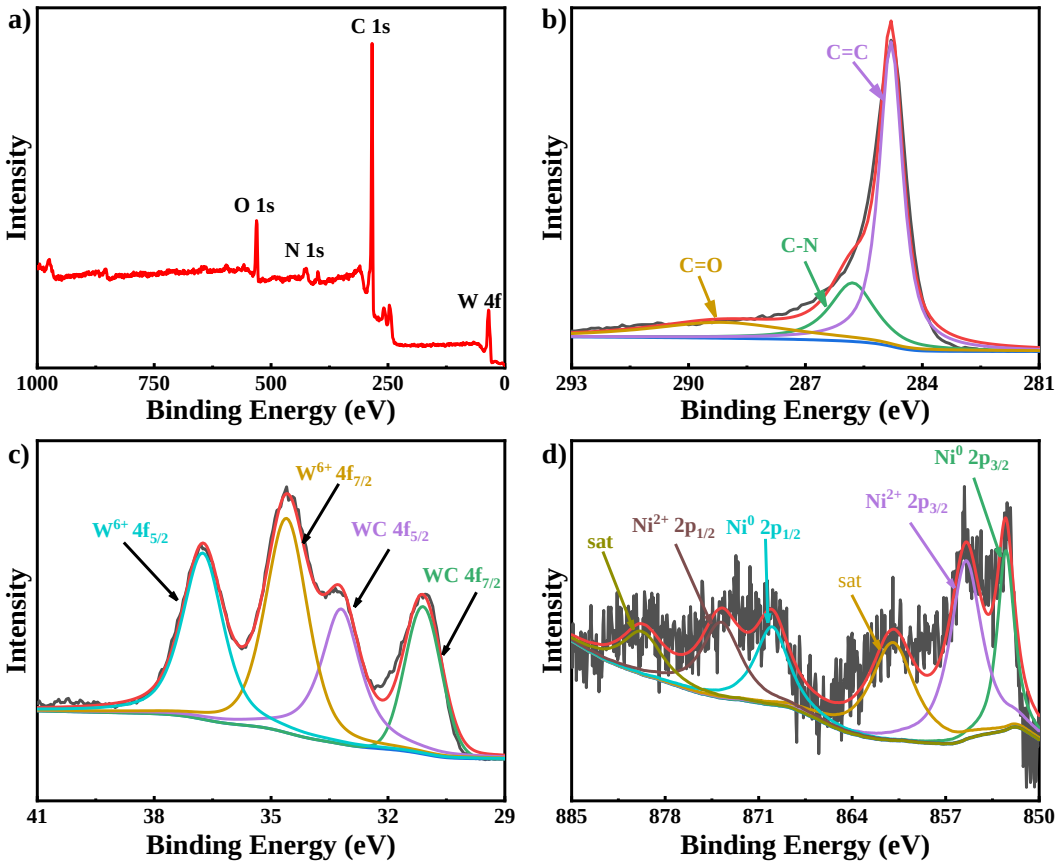

Fig. S13 (a) The survey XPS spectrum of Ni/WC@C; the high-resolution (b) C 1s, (c) W 4f and (d) Ni 2p XPS spectra of Ni/WC@C.

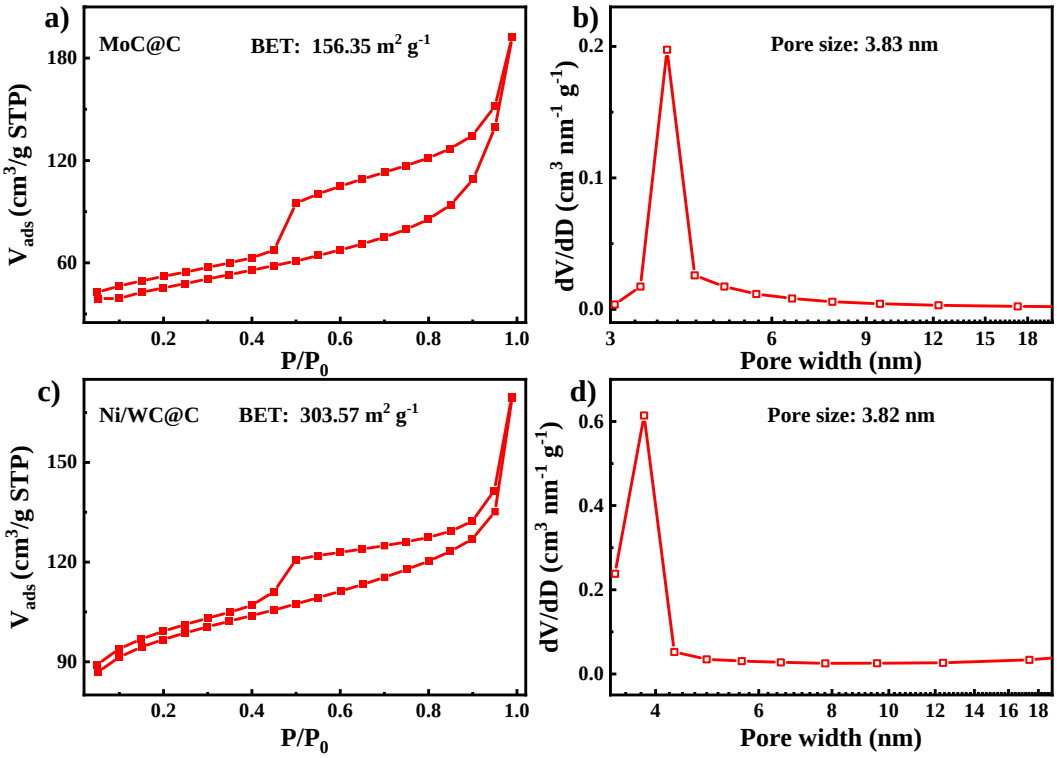

Fig. S14 N_2 sorption isotherms of (a) MoC@C, (b) Ni/WC@C, and Pore size distributions of (c) MoC@C, (d) Ni/WC@C.

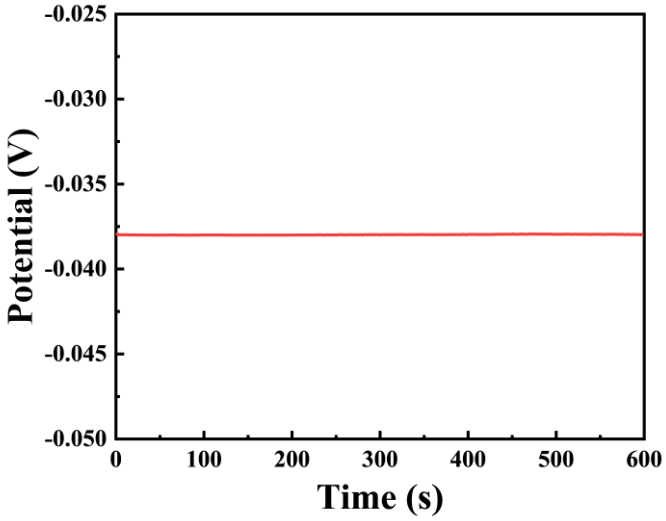

Fig. S15 Open circuit potential (OCP) values between Ag/AgCl and SCE.

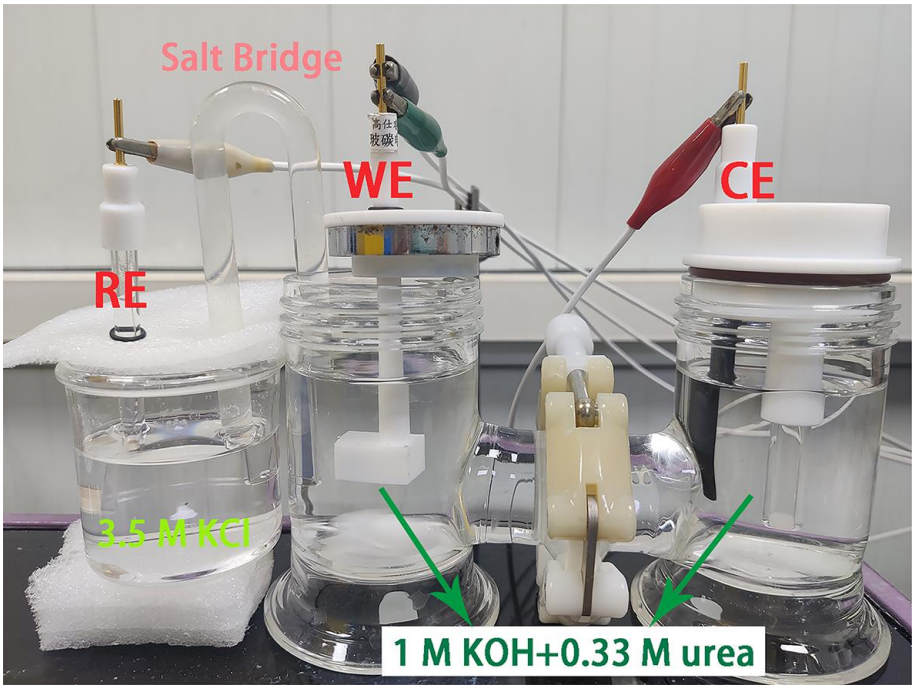

Fig. S16 Photograph of the electrochemical device containing a salt bridge for UOR.

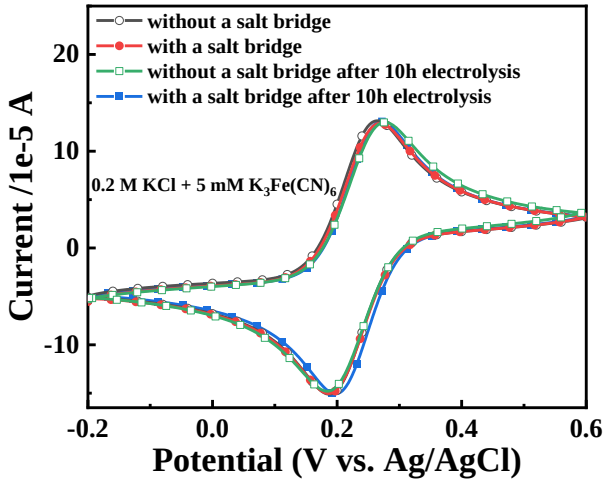

Fig. S17 Comparison of CV curves of potassium ferricyanide (5 mM $K_3Fe(CN)_6$) with and without a salt bridge (scan rate: 50 mV/s).

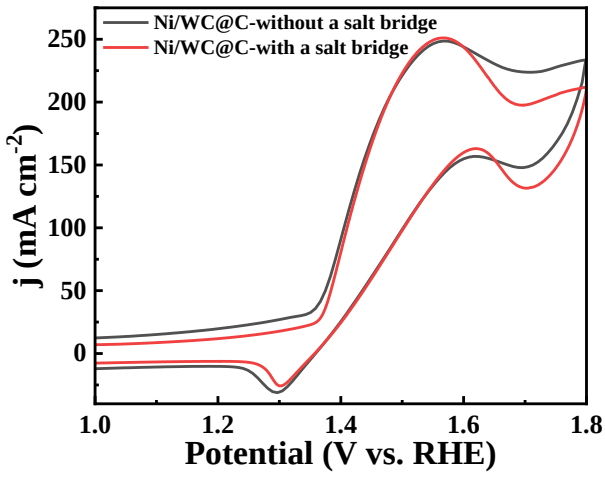

Fig. S18 Comparison of CV curves of Ni/WC@C in 1 M KOH + 0.33 M urea solution with (red) and without (black) a salt bridge (scan rate: 50 mV/s).

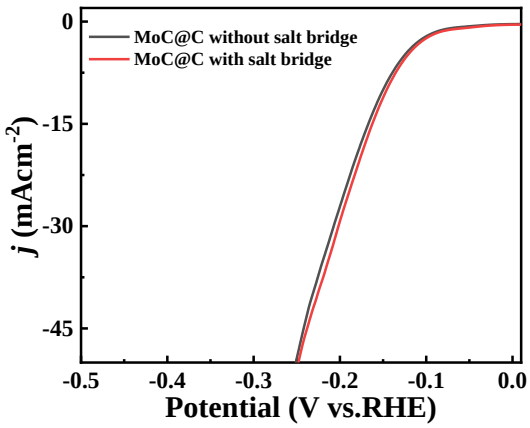

Fig. S19 Comparison of LSV curves of MoC@C in 1M KOH solution with (red) and without (black) a salt bridge (scan rate: 5 mV/s).

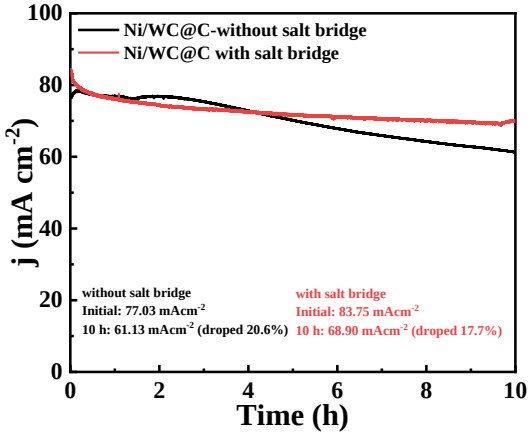

Fig. S20 Chronoamperograms of Ni/WC@C at 1.45 V (*vs*. RHE) with (red) and without (black) a salt bridge.

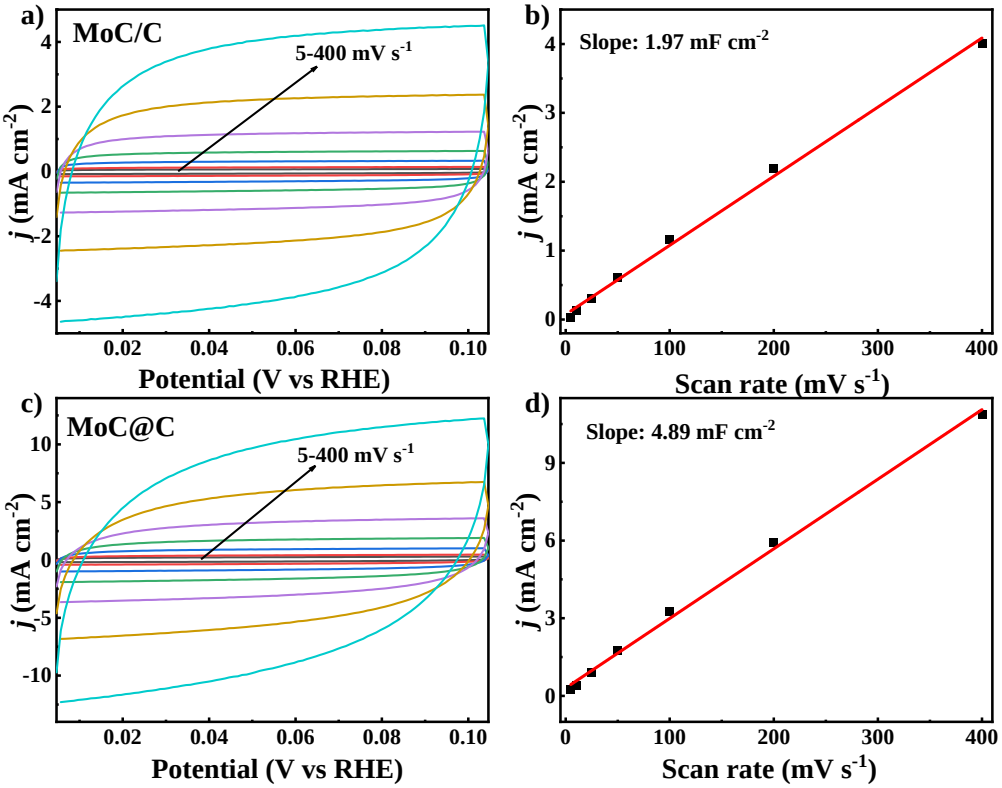

Fig. S21 (a) CVs of MoC/C with different rates from 5 to 400 mV s^{-1}, (b) Linear fitting of current densities and scan rates at a given potential of 0.05 V *vs.* RHE, (c) CVs of MoC@C with different rates from 5 to 400 mV s^{-1}, (d) Linear fitting of current densities and scan rates at a given potential of 0.05 V *vs.* RHE.

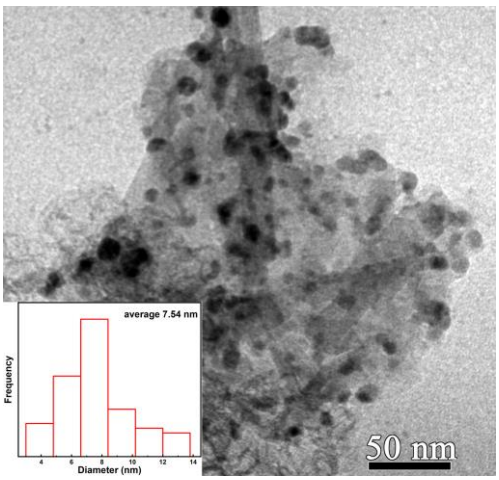

Fig. S22 TEM image of MoC/C, (inset: particle size distribution).

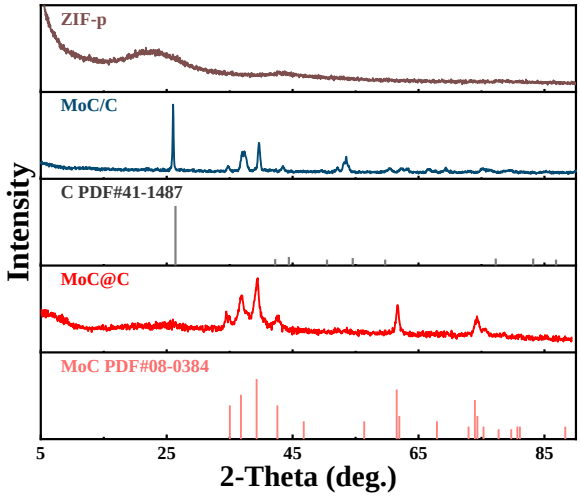

Fig. S23 XRD patterns of MoC@C, MoC/C and ZIF-p.

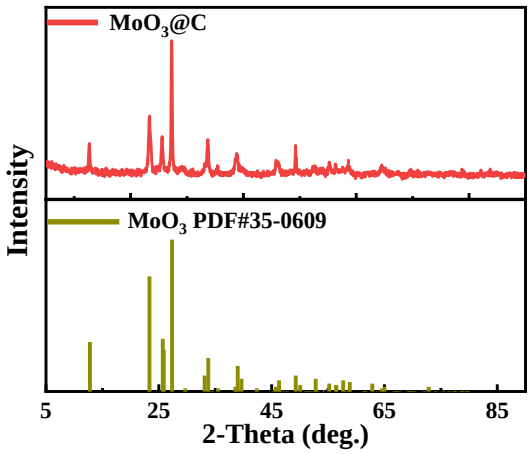

Fig. S24 XRD pattern of MoO_3@C.

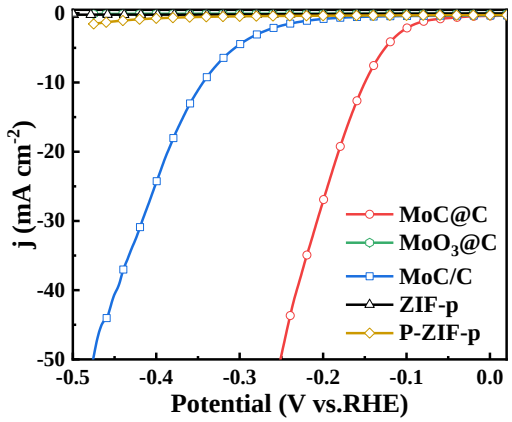

Fig. S25 LSV curvers of MoC@C, MoO_3@C, MoC/C, ZIF-p and P-ZIF-p in 1 M KOH solution (scan rate: 5 mV/s). **[As mentioned in article, there are detectable Mo(VI) species in the MoC@C sample based on the XPS results, and it may influence the catalytic behavior of MoC@C. To address this issue, the assynthesized MoC@C was oxidized to MoO_3@C, and then we examined its HER activity in an alkaline solution. As a result, the HER activity of MoO_3@C is negligible.]**

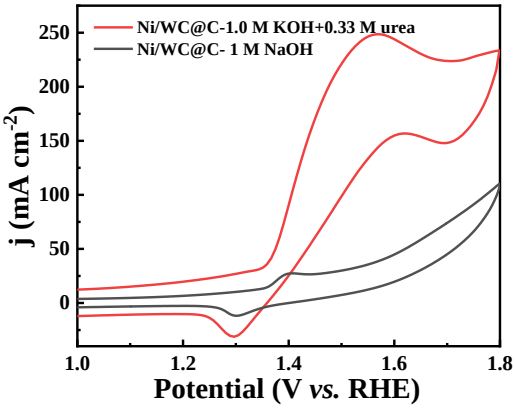

Fig. S26 CV curves of Ni/WC@C in 1 M KOH + 0.33 M urea and 1 M KOH solution. [**Based on the CV tests, it can be concluded that Ni/WC@C only exhibits UOR activity after the surface reconstruction of Ni(II) into Ni(III), indicating Ni(III) is the UOR catalytic center of Ni/WC@C.**]

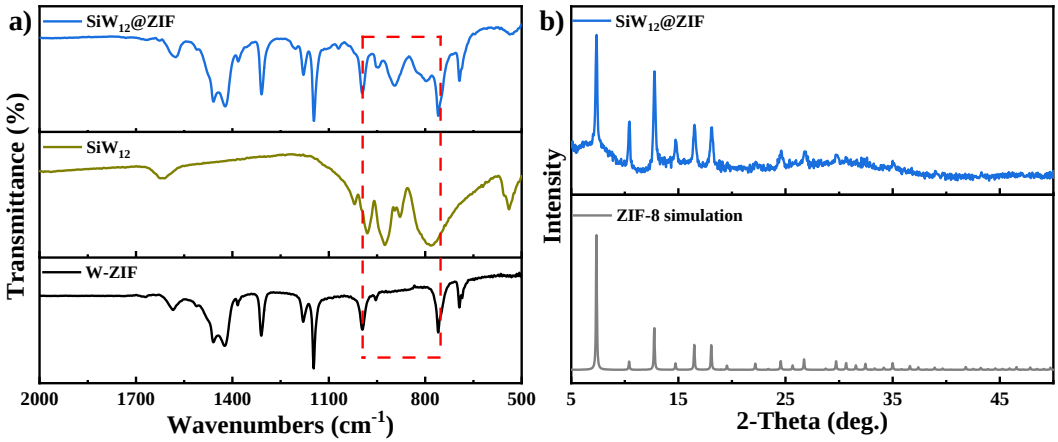

Fig. S27 (a) IR spectra of W-ZIF, SiW_{12} and SiW_{12}@ZIF, (b) XRD patterns of ZIF-8 simulation and SiW_{12}@ZIF.

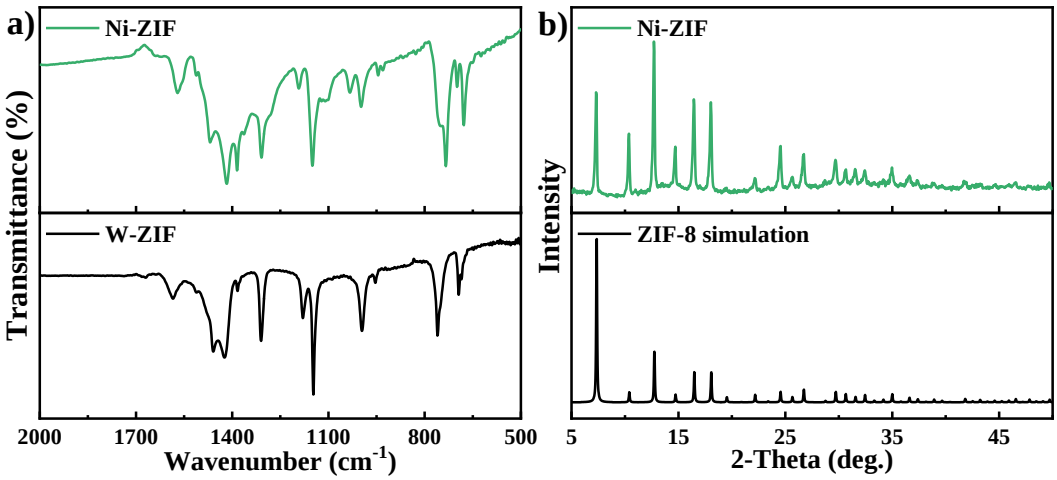

Fig. S28 (a) IR spectrums of W-ZIF and Ni-ZIF, (b) XRD patterns of ZIF-8 simulation and Ni-ZIF.

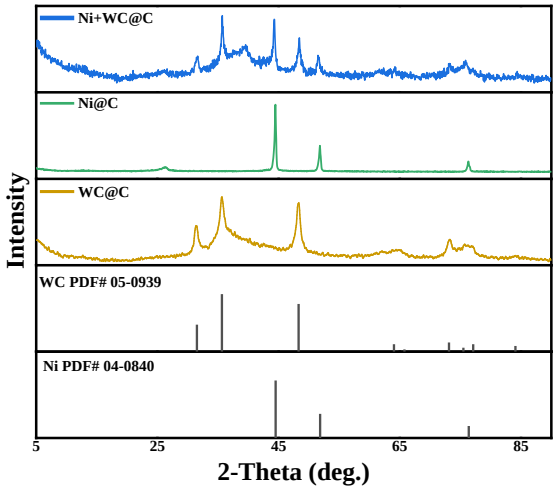

Fig. S29 XRD patterns of WC@C, Ni@C, and Ni+WC@C.

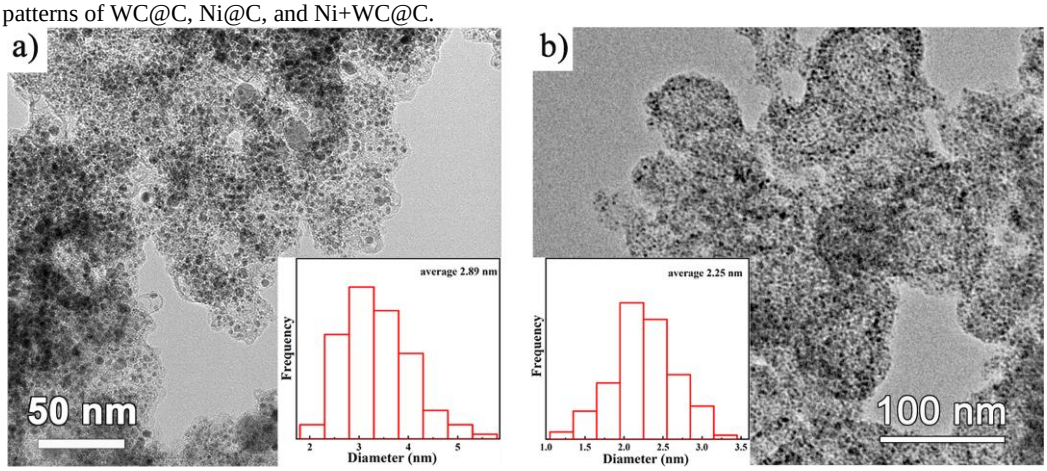

Fig. S30 TEM images of (a) Ni+WC@C, (b) WC@C (inset: particle size distribution).

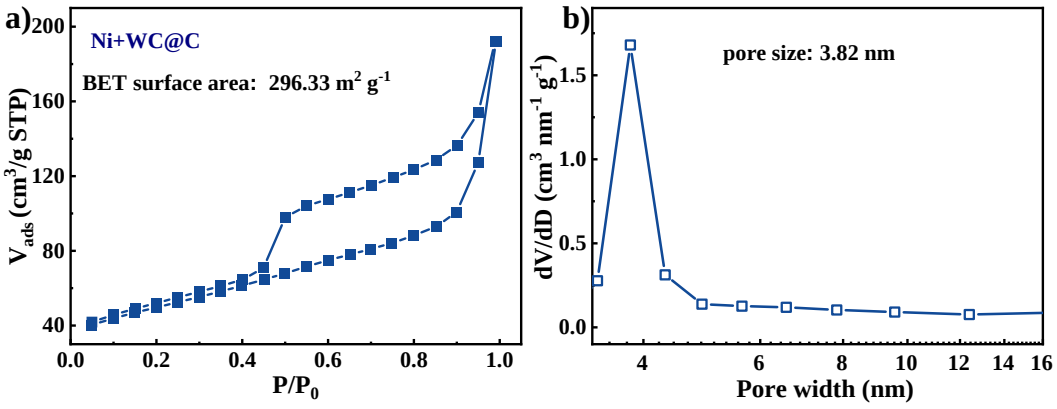

Fig. S31 (a) N_2 sorption isotherm of Ni+WC@C, (b) Pore size distribution of Ni+WC@C.

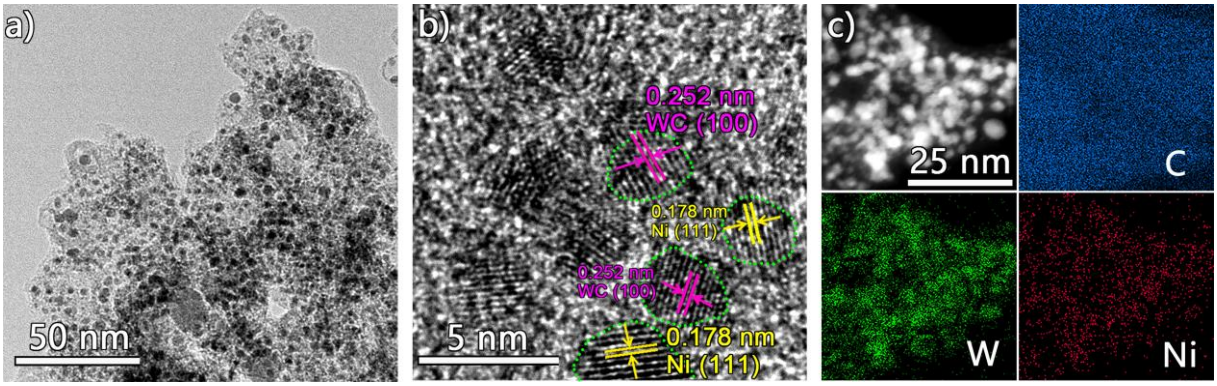

Fig. S32 (a) TEM, (b) HRTEM, and (c) EDX elemental mapping images of Ni+WC@C.

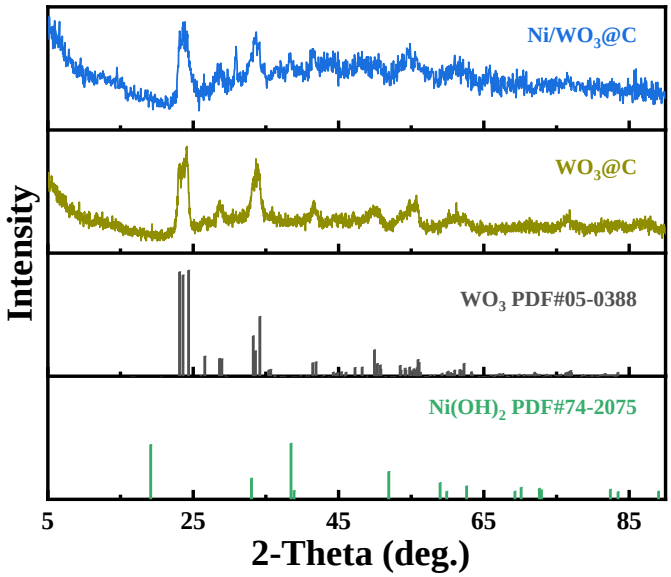

Fig. S33 XRD patterns of WO_3@C and Ni/WO_3@C.

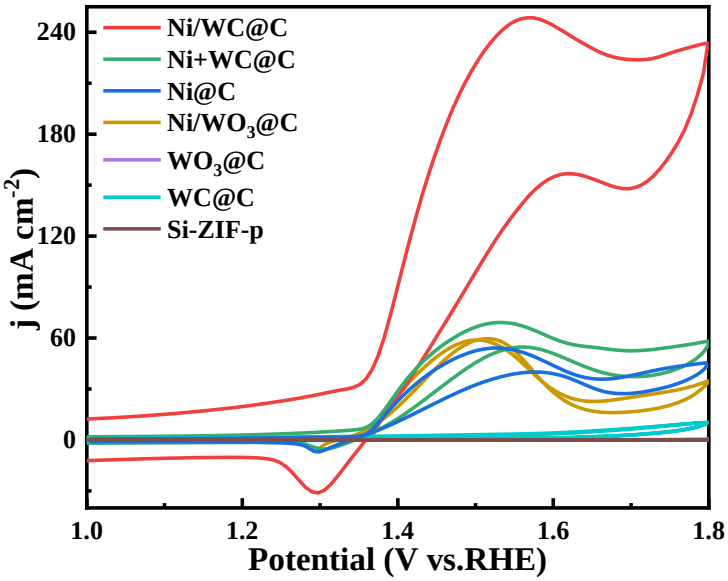

Fig. S34 CV curves of Ni/WC@C, Ni+WC@C, Ni@C, WC@C, Ni/WO_3@C, WO_3@C, and Si-ZIF-p in 1 M KOH + 0.33 M urea solution (scan rate: 50 mV/s).

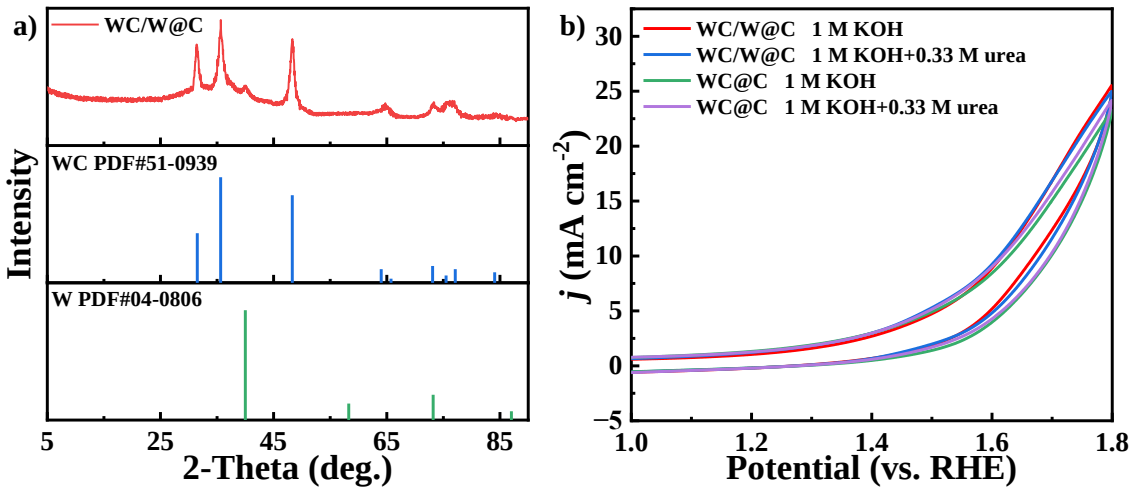

Fig. S35 (a) XRD pattern of WC/W@C, (b) CV curves of WC/W@C and WC@C in 1 M KOH with and without 0.33 M urea. (in **Fig. S35**, we could find that the CV curves of WC/W@C and WC@C are similar, so we believe the trace amount of W has no UOR activity,)

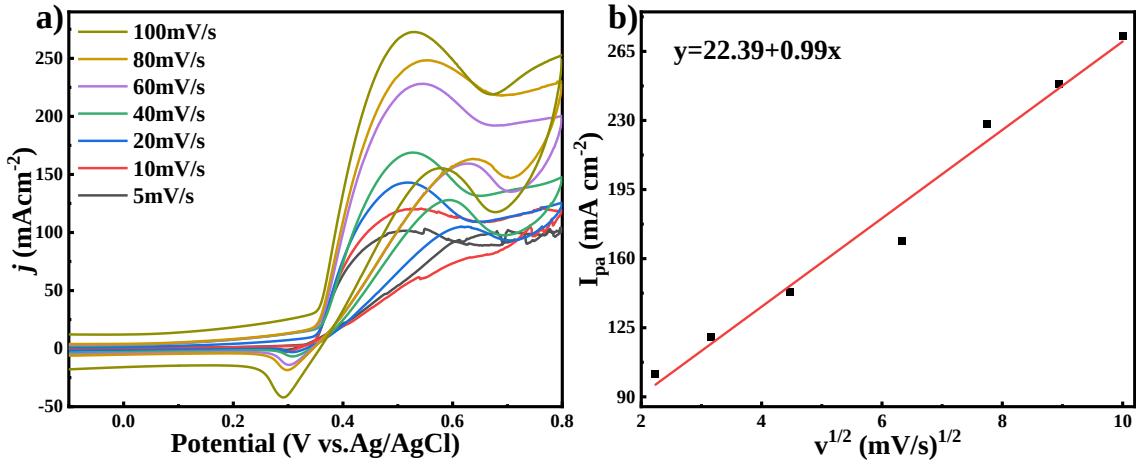

Fig. S36 (a) CVs of Ni/WC@C in 1 M KOH + 0.33 M urea using different scan rate (5, 10, 20, 40, 60, 80 and 100 mV s^{-1}), (b) Relationship between the oxidation peak current densities and the scan rate.

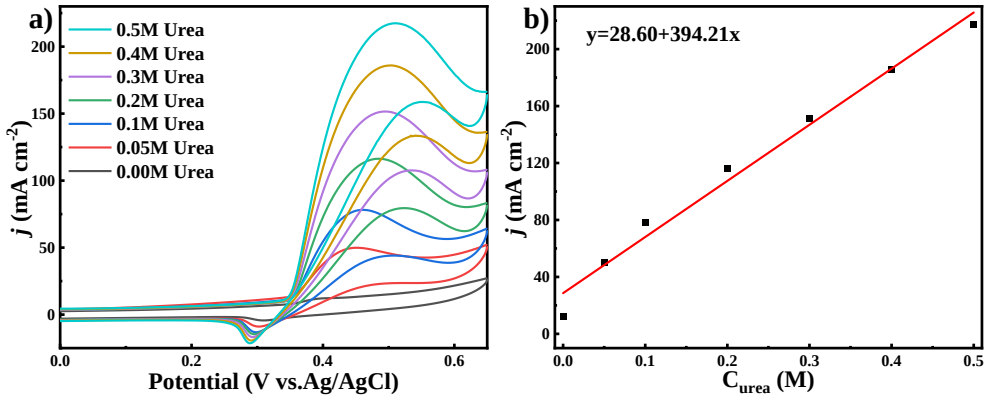

Fig. S37 (a) CV curves of Ni/WC@C in 1 M KOH solution with different urea concentrations (scan rate of 50 mV s^{-1}), (b) Relationship between the oxidation peak current densities and the urea concentrations.

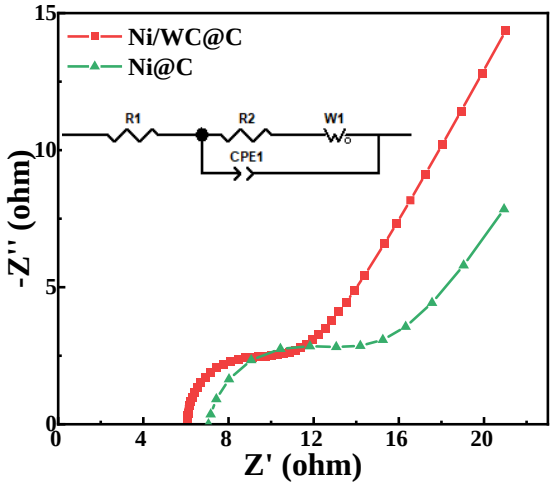

Fig. S38 The EIS of Ni/WC@C and Ni@C catalyst.

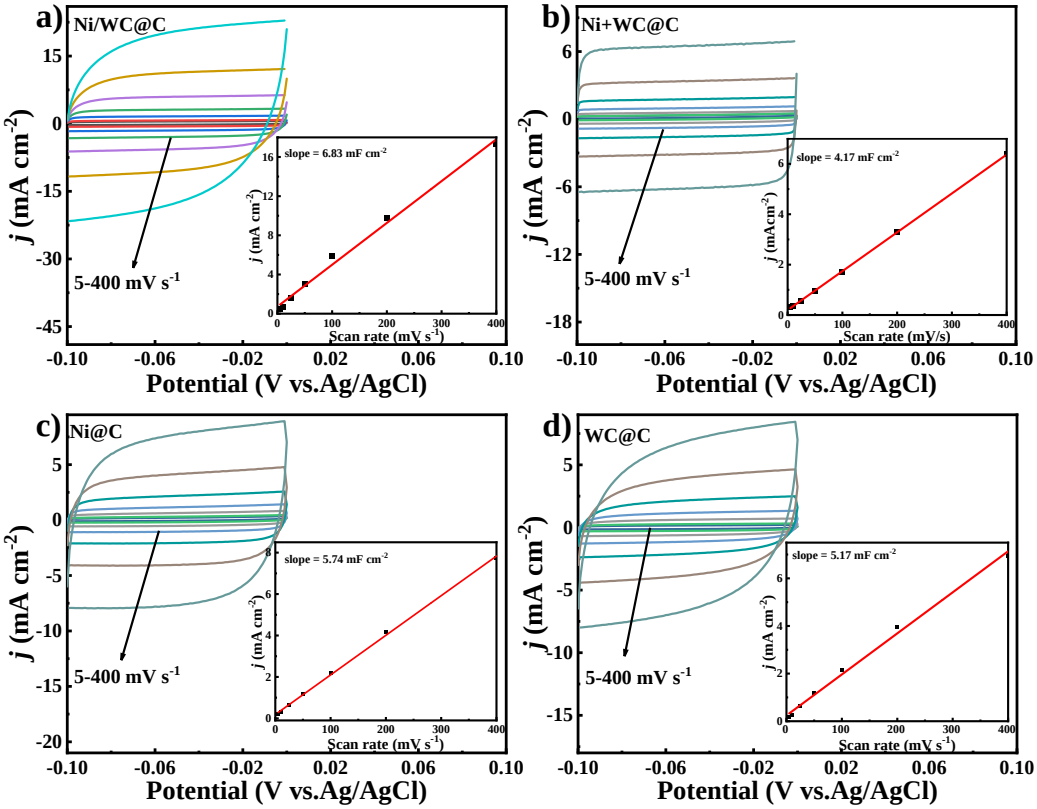

Fig. S39 CV curves of (a) Ni/WC@C, (b) Ni+WC@C, (c) Ni@C and (d) WC@C samples with different rates from 5 to 400 mV s^{-1}. (The capacitive current at -0.05 V as a function of scan rate for the corresponding samples).

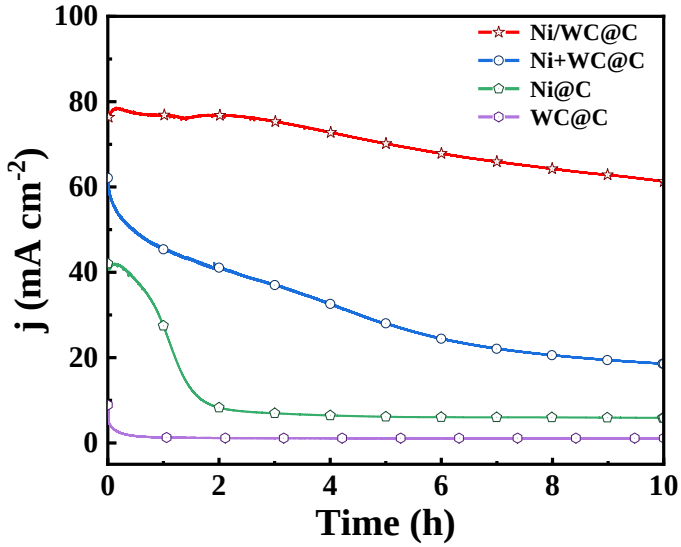

Fig. S40. Chronoamperograms of Ni/WC@C, Ni+WC@C, Ni@C and WC@C.

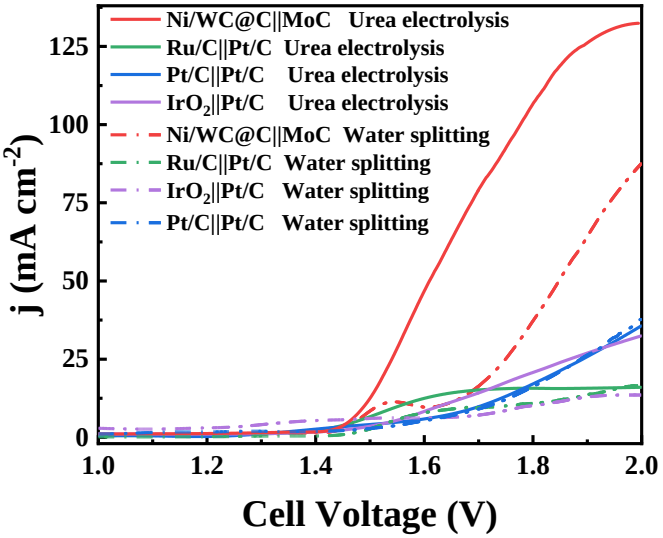

Fig. S41 Polarization curves of Ni/WC@C||MoC@C, Ru/C||Pt/C, Pt/C||Pt/C and IrO_2||Pt/C in 1 M KOH + 0.33 M urea and 1 M KOH electrolyte (scan rate: 5 mV/s).

Table S1 Calculating the size of MoC from XRD

2θ	*hkl*	θ	β	D (nm)
34.75	(101)	17.38	0.449	**3.0**
36.54	(006)	18.27	0.061	**2.7**
39.37	(103)	19.68	0.070	**2.9**
42.63	(104)	21.32	0.065	**2.7**
46.76	(105)	23.38	0.317	**2.4**
56.38	(107)	28.19	0.048	**2.8**
61.61	(110)	30.81	0.072	**2.3**
67.90	(109)	33.95	0.058	**2.9**
72.96	(201)	36.48	0.181	**2.2**

Table S2 Calculating the size of Ni/WC from XRD

2θ	*hkl*	θ	β	D (nm)
31.37	(001)	15.68	0.049	**2.8**
35.56	(100)	17.78	0.136	2.1
44.05	(111)	22.02	0.050	2.5
48.38	(101)	24.19	0.212	1.1
64.05	(110)	32.02	0.083	2.0
73.18	(111)	36.59	0.114	2.7
75.47	(200)	37.73	0.057	2.4
77.20	(102)	38.60	0.109	2.0
84.13	(201)	42.06	0.153	2.6

Table S3 The element analysis of as-synthesized samples

Samples	Atomic contents (wt%)								
	C	H	N	Zn	Mo	W	Ni	P	Si
ZIF-8	47.98	6.23	22.65	23.09	/	/	/	/	/
O-ZIF	50.21	3.30	14.79	21.16	/	/	/	/	/
PMo_{12}@ZIF	31.54	3.87	16.58	23.47	18.62	/	/	/	/
PMo_{12}/ZIF	32.33	4.01	15.68	22.29	19.49	/	/	/	/
MoC@C	24.99	1.40	2.51	0.60	66.67	/	/	0.49	/
MoC/C	23.36	1.68	2.68	0.24	71.64	/	/	0.37	/
W-ZIF	48.07	6.44	22.64	22.70	/	/	/		/
SiW_9Ni_3@ZIF	36.56	4.62	17.68	18.53	/	12.91	1.46	/	/
SiW_{12}@Ni-ZIF	37.23	4.29	16.06	16.23	/	13.80	1.58	/	/
Ni/WC@C	47.28	1.16	2.43	/	/	38.56	8.13	/	0.82
Ni+WC@C	47.73	0.89	2.66	/	/	37.98	7.67	/	0.17
Ni@C	61.05	2.51	9.73	/	/	/	8.60	/	/
WC@C	48.65	1.26	2.81	/	/	40.03	/	/	0.65
Si-ZIF-p	78.13	0.67	15.98	0.91	/	/	/	/	0.77
P-ZIF-p	71.25	2.05	15.05		/	/	/	0.73	/
ZIF-p	77.21	0.53	16.32	4.36	/	/	/	/	/

Table S4 Catalytic activity Comparison of the Ni/WC@C and other UOR catalysts reported in the literatures

Catalysts	Condition	Onset potential (V *vs.* RHE)	Peak potential (V *vs.* RHE)	Specific activity (mA cm^{-2})	Mass activity (mA mg^{-1})	References
Ni/WC@C	**1 M KOH + 0.33 M urea**	**1.35**	**1.55**	**248**	**1012**	**This work**
$NiCo_2S_4$@CS	5 M KOH + 0.2 M urea	1.17	1.53	673	/	[13]
Ni-WOx	1 M KOH + 0.33 M urea	1.35	1.60	440	/	[14]
β-$Ni(OH)_2$/SSM	1 M KOH + 0.33 M urea	1.37	1.8	250	/	[15]
Au/NiCo-LDH	1 M KOH + 0.33 M urea	1.15	1.42	141.5	/	[16]
P-NTS-0.5	1 M KOH + 0.33 M urea	1.33	1.6	126	/	[17]
Pd/NiCo-LDH	1 M KOH + 0.33 M urea	1.15	1.42	104.3	/	[16]
Ag/NiCo-LDH	1 M KOH + 0.33 M urea	1.15	1.42	72	/	[16]
NiCo-LDH	1 M KOH + 0.33 M urea	1.18	1.42	51	/	[16]
Ir_3Sn/FeNC	5 M KOH + 0.33 M urea	1.25	1.28	/	157	[18]
$Ni(OH)_2$-NMs	1 M KOH + 0.33 M urea	1.35	1.55	/	408.3	[19]
Ni_2P	1 M KOH + 0.5 M urea	1.33	1.60	95.47	/	[20]
Pt/C	1 M KOH + 0.33 M urea	ca. 1.40	ca. 1.55	25	/	[21]

Table S5 Comparison of stability between the Ni/WC@C and other UOR [a] catalysts reported in the literature

Catalysts	Condition	Fix potential	Test time	Initinal	Decrease	Ref
M-$Ni(OH)_2$ nanosheets	1 M KOH + 0.33 M urea	0.46 V vs. Ag/AgCl	10 h	18 mA cm^{-2}	2%	[22]
NiO-NiPi	1 M KOH + 0.5 M urea	1.38 V vs. RHE	10 h	100mAcm-$^{-2}$	2.6%	[23]
$NiTe_2$/$Ni(OH)_2$/CFC	1 M KOH + 0.33 M urea	1.39 V vs. RHE	10h	10 mAcm^{-2}	3%	[24]
NF/NiMoO-Ar	1 M KOH + 0.5 M urea	1.4 V vs. RHE	10 h	83 mAcm^{-2}	7%	[25]
HC-NiMoS precursor/Ti	1 M KOH + 0.5 M urea	0.34 V vs. RHE	10 h	19 mAcm^{-2}	11.6%	[26]
NF-G-Mn	1 M KOH + 0.5 M urea	0.35 V vs. Ag/AgCl	10 h	9 mAcm^{-2}	16%	[27]
Ni/WC@C	**1 M KOH + 0.33 M urea**	**1.45 V *vs.* RHE**	**10 h 3 h 2h 1h**	**77 mA cm^{-2} 77 mA cm^{-2} 77 mA cm^{-2} 77 mA cm^{-2}**	**20% 2.2% 0.31% 0.28%**	**This work**
Ni/Mo_2C@CN-6	1 M KOH + 0.5 M urea	1.4 V vs. RHE	10 h	14 mAcm^{-2}	21%	[28]
FQD/CoNi-LDH/NF	1 M KOH + 0.5 M urea	1.4 V vs. RHE	10 h	15 mAcm^{-2}	28%	[29]
SL $Ni(OH)_2$ NS/CC	1 M KOH + 0.33 M urea	0.5 V vs. Ag/AgCl	10 h	350 mA cm^{-2}	41%	[30]
Co(OH)F	1 M KOH + 0.7 M urea	1.25 V vs. RHE	10 h	15 mA cm^{-2}	50%	[31]
NiF_3/Ni_2P	1 M KOH + 0.33 M urea	1.36 V vs. RHE	10 h	10 mAcm^{-2}	70%	[32]
NF@NiO-450	1 M KOH + 0.33 M urea	0.45 V vs. SCE	3 h	50 mA cm^{-2}	24%	[33]
N-NiS/NiS_2	1 M KOH + 0.33 M urea	1.38 V vs. RHE	2 h	10 mAcm^{-2}	4%	[34]
$Ni(OH)_2$-NMs	1 M KOH + 0.33 M urea	1.48 V vs. RHE	1.67 h (6000s)	180 mA mg^{-1}	17.67%	[19]
$MnCo_2O_{4.5}$@$Ni(OH)_2$/NF	5 M KOH + 0.33 M urea	0.46 V vs. Ag/AgCl	1 h	400 mAcm^{-2}	12.5%	[35]
Ni nanowires	1 M KOH + 0.33 M urea	0.55 V vs. Hg/HgO	1.53 h (5500 s)	20 mA cm^{-2}	65%	[36]
$Ni(OH)_2$ nanoribbon	5 M KOH + 0.33 M urea	0.5 V vs. Hg/HgO	1 h	4 mA cm^{-2} mg^{-1}	31%	[37]
Ni-WC/C	1 M KOH + 0.33 M urea	0.5 V vs. Hg/HgO	1 h	350 mA mg^{-1}	71%	[38]
Bulk $Ni(OH)_2$ powder	5 M KOH + 0.33 M urea	0.5 V vs. Hg/HgO	1 h	0.3 mA cm^{-2} mg^{-1}	40%	[37]
β $Ni(OH)_2$	1 M KOH + 0.33 M urea	1.48 V vs. RHE	0.83 h (3000 s)	1.25 mA cm^{-2}	31%	[39]
Ni/$Ni(OH)_2$	1 M KOH + 0.33 M urea	1.48 V vs. RHE	0.83 h (3000 s)	1 mA cm^{-2}	40%	[39]
$NiMoO_4$-C	1 M KOH + 0.33 M urea	0.35 V vs. SCE	0.44 h (1600 s)	17 mA cm^{-2}	17%	[40]
$LaNiO_3$	5 M KOH + 0.33 M urea	0.45 V vs. Hg/HgO	0.33 h (1200 s)	600 mA mg^{-1}	83%	[41]
Ni-Mo/G	1 M KOH + 0.33 M urea	0.5 V vs. Ag/AgCl	0.28 h (1000 s)	90 mA cm^{-2}	24%	[42]
$Ni_{1.5}Mn_{1.5}O_4$	1 M KOH + 0.33 M urea	0.5 V vs Ag/AgCl	0.28 h (1000 s)	30 mA cm^{-2}	33%	[43]
NiMn-CNFs	1 M KOH + 2 M urea	0.6 V *vs.* Ag/AgCl	0.25 h (900 s)	300 mA cm^{-2} g^{-1}	57%	[44]

Note: UOR [a]: urea oxidation reaction; Ref: Reference.

Table S6 Faraday Efficiency (FE) Comparison of this work and other UOR catalysts reported in the literature

Anode materials	Compositions of electrolyte solution	FE of Urea electrolysis	Reference
Ni/WC@C	**1.0 M KOH + 0.33 M urea**	**82.2% (N_2)**	**This work**
MoC@C	**1.0 M KOH + 0.33 M urea**	**90% (H_2)**	**This work**
C@FeNi	1.0 M KOH + 0.05 M urea	56% (N_2)	[45]
CNT/C@FeNi	1.0 M KOH + 0.05 M urea	68.4% (N_2)	[45]
NiCo/LDH-NO_3	1.0 M KOH + 0.33 M urea	21.3% (O_2)	[46]
CuO/Cu_2O@CD-CN/NiF	1.0 M Na_2SO_4 + 0.50 M urea	23.9% (NH_3)	[47]
Ni-Mo alloy nanotube	1.0 M KOH + 0.10 M urea	92% (N_2)	[48]
Cu_2S@Ni_3Se_2/Cu foam	1.0 M KOH + 0.50 M urea	92% (H_2)	[49]

Reference

1 J. Kreiter and E. E. Pohl, *J. Vis. Exp.*, 2019, 58552.
2 F. T. L. Muniz, M. A. R. Miranda, C. Morilla dos Santos and J. M. Sasaki, *Acta Crystallogr. Sect. Found. Adv.*, 2016, **72**, 385–390.
3 C. Rocchiccioli-Deltcheff, M. Fournier, R. Franck and R. Thouvenot, *Inorg. Chem.*, 1983, **22**, 207–216.
4 A. Téazéa, G. Hervéa, R. G. Finke and D. K. Lyon, in *Inorganic Syntheses*, ed. A. P. Ginsberg, John Wiley & Sons, Inc., Hoboken, NJ, USA, 2007, pp. 85–96.
5 Q. Lunyu, S. Yingji, C. Yaguang, Y. Ming and P. Jun, *Synth. React. Inorg. Met.-Org. Chem.*, 1994, **24**, 1339–1350.
6 J. Cravillon, S. Münzer, S.-J. Lohmeier, A. Feldhoff, K. Huber and M. Wiebcke, *Chem. Mater.*, 2009, **21**, 1410–1412.
7 M. Zhang, V. Singh, X. Hu, X. Ma, J. Lu, C. Zhang, J. Wang and J. Niu, *ACS Catal*, 2019, 10.
8 N. Lied, *ACS Appl Mater Interfaces*, 2012, 6.
9 H.-L. Jiang, B. Liu, Y.-Q. Lan, K. Kuratani, T. Akita, H. Shioyama, F. Zong and Q. Xu, *J. Am. Chem. Soc.*, 2011, **133**, 11854–11857.
10 G. L. Turdean, A. Patrut, L. David and I. C. Popescu, *J. Appl. Electrochem.*, 2008, **38**, 751–758.
11 A. V. Syugaev, N. V. Lyalina, S. F. Lomayeva and A. N. Maratkanova, *J. Solid State Electrochem.*, 2016, **20**, 775–784.
12 Y. Leng, L. Xie, F. Liao, J. Zheng and X. Li, *Thermochim. Acta*, 2008, **473**, 14–18.
13 B. Li, C. Song, J. Rong, J. Zhao, H.-E. Wang, P. Yang, K. Ye, K. Cheng, K. Zhu, J. Yan, D. Cao and G. Wang, *J. Energy Chem.*, 2020, **50**, 195–205.
14 L. Wang, Y. Zhu, Y. Wen, S. Li, C. Cui, F. Ni, Y. Liu, H. Lin, Y. Li, H. Peng and B. Zhang, *Angew. Chem. Int. Ed.*, 2021, **60**, 10577–10582.
15 A. A. Kashale, A. Ghule and I.-W. P. Chen, *Chemcatchem*, DOI:10.1002/cctc.202001528.
16 D. Khalafallah, L. Xiaoyu, M. Zhi and Z. Hong, *Chemelectrochem*, 2020, **7**, 163–174.
17 Z. Ji, J. Liu, Y. Deng, S. Zhang, Z. Zhang, P. Du, Y. Zhao and X. Lu, *J. Mater. Chem. A*, 2020, **8**, 14680–14689.
18 T. Tan, S. Liu, K. Chen, S. Imhanria, P. Tao and W. Wang, *J. Taiwan Inst. Chem. Eng.*, 2020, **112**, 116–121.
19 Y. Ding, Y. Li, Y. Xue, B. Miao, S. Li, Y. Jiang, X. Liu and Y. Chen, *Nanoscale*, 2019, **11**, 1058–1064.
20 H. Liu, S. Zhu, Z. Cui, Z. Li, S. Wu and Y. Liang, *Nanoscale*, 2021, **13**, 1759–1769.
21 Q. Zhang, F. MD. Kazim, S. Ma, K. Qu, M. Li, Y. Wang, H. Hu, W. Cai and Z. Yang, *Appl. Catal. B Environ.*, 2021, **280**, 119436.
22 X. Zhu, X. Dou, J. Dai, X. An, Y. Guo, L. Zhang, S. Tao, J. Zhao, W. Chu, X. C. Zeng, C. Wu and Y. Xie, *Angew. Chem. Int. Ed.*, 2016, **55**, 12465–12469.
23 X. Xu, T. Guo, J. Xia, B. Zhao, G. Su, H. Wang, M. Huang and A. Toghan, *Chem. Eng. J.*, 2021, **425**, 130514.
24 B. Xu, X. Yang, X. Liu, W. Song, Y. Sun, Q. Liu, H. Yang and C. Li, *J. Power Sources*, 2020, **449**, 227585.
25 Z.-Y. Yu, C.-C. Lang, M.-R. Gao, Y. Chen, Q.-Q. Fu, Y. Duan and S.-H. Yu, *Energy Environ. Sci.*, 2018, **11**, 1890–1897.
26 X. Wang, J. Wang, X. Sun, S. Wei, L. Cui, W. Yang and J. Liu, *Nano Res.*, 2018, **11**, 988–996.
27 S. Chen, J. Duan, A. Vasileff and S. Z. Qiao, *Angew. Chem. Int. Ed.*, 2016, **55**, 3804–3808.
28 Z. Liu, S. Xue, S. Zhou, J. Li, K. Qu and W. Cai, *J. Catal.*, 2022, **405**, 606–613.
29 Y. Feng, X. Wang, J. Huang, P. Dong, J. Ji, J. Li, L. Cao, L. Feng, P. Jin and C. Wang, *Chem. Eng. J.*, 2020, **390**, 124525.
30 C. Lin, Z. Gao, F. Zhang, J. Yang, B. Liu and J. Jin, *J. Mater. Chem. A*, 2018, **6**, 13867–13873.
31 M. Song, Z. Zhang, Q. Li, W. Jin, Z. Wu, G. Fu and X. Liu, *J. Mater. Chem. A*, 2019, **7**, 3697–3703.
32 K. Wang, W. Huang, Q. Cao, Y. Zhao, X. Sun, R. Ding, W. Lin, E. Liu and P. Gao, *Chem. Eng. J.*, 2022, **427**, 130865.
33 M.-S. Wu, F.-Y. Chen, Y.-H. Lai and Y.-J. Sie, *Electrochimica Acta*, 2017, **258**, 167–174.
34 H. Liu, Z. Liu, F. Wang and L. Feng, *Chem. Eng. J.*, 2020, **397**, 125507.
35 L. Sha, K. Ye, J. Yin, K. Zhu, K. Cheng, J. Yan, G. Wang and D. Cao, *Chem. Eng. J.*, 2020, **381**, 122603.
36 W. Yan, D. Wang, L. A. Diaz and G. G. Botte, *Electrochimica Acta*, 2014, **134**, 266–271.
37 D. Wang, W. Yan, S. H. Vijapur and G. G. Botte, *J. Power Sources*, 2012, **217**, 498–502.
38 L. Wang, S. Zhu, N. Marinkovic, S. Kattel, M. Shao, B. Yang and J. G. Chen, *Appl. Catal. B Environ.*, 2018, **232**, 365–370.
39 R. K. Singh and A. Schechter, *Electrochimica Acta*, 2018, **278**, 405–411.
40 D. Yang, L. Yang, L. Zhong, X. Yu and L. Feng, *Electrochimica Acta*, 2019, **295**, 524–531.
41 R. P. Forslund, J. T. Mefford, W. G. Hardin, C. T. Alexander, K. P. Johnston and K. J. Stevenson, *ACS Catal.*, 2016, **6**, 5044–5051.
42 W. Shi, R. Ding, X. Li, Q. Xu and E. Liu, *Electrochimica Acta*, 2017, **242**, 247–259.
43 S. Periyasamy, P. Subramanian, E. Levi, D. Aurbach, A. Gedanken and A. Schechter, *ACS Appl. Mater. Interfaces*, 2016, **8**, 12176–12185.
44 N. A. M. Barakat, M. H. El-Newehy, A. S. Yasin, Z. K. Ghouri and S. S. Al-Deyab, *Appl. Catal. Gen.*, 2016, **510**, 180–188.
45 A. Modak, R. Mohan, K. Rajavelu, R. Cahan, T. Bendikov and A. Schechter, *ACS Appl. Mater. Interfaces*, 2021, **13**, 8461–8473.
46 M. Zeng, J. Wu, Z. Li, H. Wu, J. Wang, H. Wang, L. He and X. Yang, *Acs Sustain. Chem. Eng.*, 2019, **7**, 4777–4783.
47 Y. Hou, N. Deng, F. Han, X. Kuang and X. Zheng, *Catal. Sci. Technol.*, 2020, **10**, 7819–7823.
48 J.-Y. Zhang, T. He, M. Wang, R. Qi, Y. Yan, Z. Dong, H. Liu, H. Wang and B. Y. Xia, *Nano Energy*, 2019, **60**, 894–902.
49 L. Lv, Z. Li, H. Wan and C. Wang, *J. Colloid Interface Sci.*, 2021, **592**, 13–21.